Femtosecond real-time probing of reactions. XXI. Direct observation of transition-state dynamics and structure in charge-transfer reactions

P. Y. Cheng, D. Zhong, and Ahmed H. Zewail

Citation: The Journal of Chemical Physics **105**, 6216 (1996); doi: 10.1063/1.472478
View online: http://dx.doi.org/10.1063/1.472478
View Table of Contents: http://scitation.aip.org/content/aip/journal/jcp/105/15?ver=pdfcov
Published by the AIP Publishing

Femtosecond real-time probing of reactions. XXI. Direct observation of transition-state dynamics and structure in charge-transfer reactions

P. Y. Cheng, D. Zhong, and Ahmed H. Zewail
Arthur Amos Noyes Laboratory of Chemical Physics, California Institute of Technology, Pasadena, California 91125

(Received 23 April 1996; accepted 2 July 1996)

This paper in the series gives our full account of the preliminary results reported in a communication [Cheng, Zhong, and Zewail, J. Chem. Phys. **103**, 5153 (1995)] on real-time femtosecond (fs) studies of the transition state of charge-transfer (CT) reactions, generally described as harpooning reactions. Here, in a series of experimental studies in a molecular beam, and with the help of molecular dynamics, we elucidate the microscopic elementary dynamics and the structure of the transition states for the isolated, bimolecular reaction of benzenes (electron donor) with iodine (electron acceptor). The transition state is directly reached by fs excitation into the CT state of the complex $Bz\cdot I_2$, and the dynamics is followed by monitoring the product build up or the initial transition-state decay. We further employed the fs resolution in combination with the kinetic-energy resolved time-of-flight and recoil anisotropy techniques to separate different reaction pathways and to determine the impact geometry. Specifically, we have studied: (1) the temporal evolution of the transition state ($\tau^{\ddagger}$) and of the final products (τ); (2) the product translational-energy distributions; (3) the recoil anisotropy (β) in each channel; (4) the reaction time dependence on the total energy; (5) the dynamical and structural changes with varying CT energy (ionization potential–electron affinity–Coulomb energy). Such a change is made by replacing the electron donor from benzene to toluene, and to xylenes and trimethylbenzenes of different symmetries. We have also studied deutrobenzene as a donor. The reaction mechanism involves two exit channels. The first one (ionic) follows the ionic potential of the CT state. Following the harpooning ($Bz^+\cdot I_2^-$), the transition state $[Bz^+\cdot\cdot I^-\cdot\cdot I]^{*\ddagger}$ evolves on the adiabatic potential to produce $Bz^+\cdot I^-$ and I products. The second channel (neutral) is due to the coupling of the transition state to neutral, locally excited, iodine repulsive states and, in this case, the products are $Bz\cdot I+I$. The latter process is an intermolecular electron transfer and occurs on an ultrafast time scale of 250 fs, resulting in a greater yield for the neutral channel. Molecular dynamics simulations support this dynamical picture and provide the time scales for trajectories in the transition-state region and in the product valley. The geometry of the transition state is determined from the anisotropy measurements and we found a nearly axial geometry with the iodine axis of recoil tilted 30°–35° away from the transition moment. These angular dependencies are related to the molecular structure and the electronic structure with highest occupied molecular orbit–lowest occupied molecular orbit descriptions. By increasing the level of solvation from the 1:1 complex structure to clusters, we address the dynamics of caging in small and large solvent structures. We also report studies in the liquid phase and compare our results with those from other laboratories in an attempt to unify the nature of the dynamics and structure in going from the isolated gas phase complex to the liquid. © *1996 American Institute of Physics.* [S0021-9606(96)01438-9]

I. INTRODUCTION

Charge-transfer (CT) reactions play a central role in many areas of chemistry and biology. Common to all CT reactions is the coupling between ionic and covalent (neutral) configurations which establishes a unique transition state. The transition state is a hybrid of these ionic and covalent structures with an ultrafast interconversion (usually less than a picosecond), accompanied by bond breakage and bond formation. A generic description of bimolecular charge-transfer reactions of $A+BC$ (or A^*+BC) is illustrated schematically in Fig. 1.

In the entrance channel the system converts from being covalent to being ionic in nature by utilizing the harpooning mechanism at long internuclear separations. The near degeneracy of the covalent and ionic energies facilitates such transformation, even at the long distances of 5–10 Å (entrance channel). In the transition state, the CT establishes the structure $[A^+\cdot\cdot{}^-BC]$ over a range of distances. Ultimately, in the exit channel, the transition state (TS) either continues on the adiabatic harpoon potential, utilizing the coulomb attraction to form A^+B^-+C, or searches for the covalent channel of $AB+C$. The elementary steps involved are

$$A+BC\rightarrow[A^+\cdot\cdot{}^-B\cdot\cdot C]^{\ddagger}\rightarrow A^+B^-+C \quad \text{(ionic channel)} \tag{1}$$

$$\rightarrow AB+C \quad \text{(neutral channel)}. \tag{2}$$

The TS can be reached thermally from the entrance channel or directly by a photon excitation.

 0021-9606/96/105(15)/6216/33/$10.00

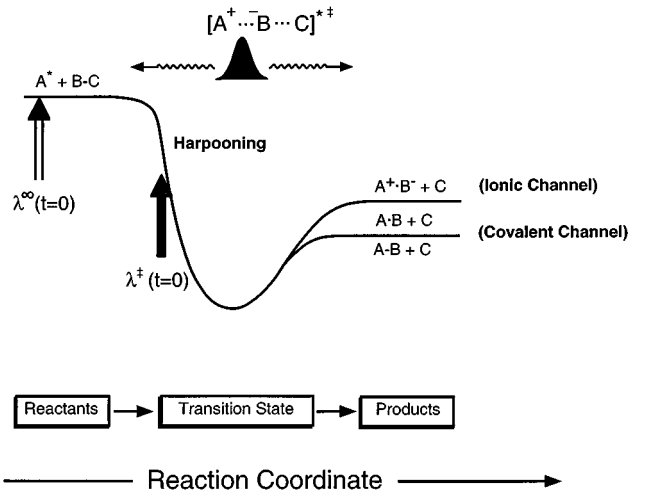

FIG. 1. The reaction path relevant to charge–transfer reactions and the concept of the approach presented in this work. The reaction path in these type of reactions involve both the ionic and covalent potentials, as shown for the present systems in Figs. 3, 22, and 25. The transition state $[A^+\cdots{}^-B\cdots C]^{*\ddagger}$, which is a hybrid of the ionic and covalent configurations, can be reached by harpooning at the covalent–ionic intersection in the entrance channel (reactants), or by direct fs excitation at $t=0$ from the ground state through CT transition (the initial ground state is not shown). The reaction then proceeds through ionic and/or covalent channels depending on the nature of the transition state. The solid arrow indicates the initial preparation of the harpoon region from the van der Waals ground state configuration $[A\cdots B\cdots C]^{\ddagger}$. The hollow arrow represents the preparation through one of the reagents at large internuclear separation.

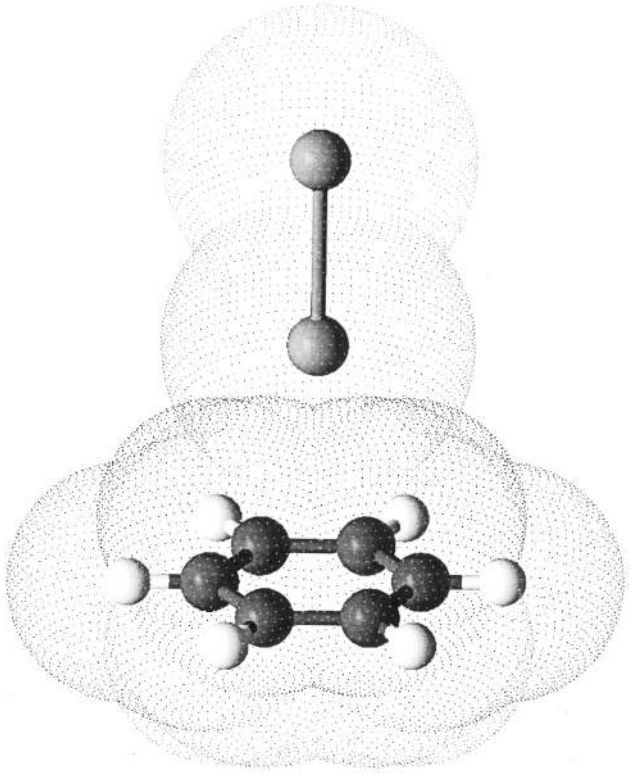

FIG. 2. Molecular structure of $Bz\cdot I_2$ based on the results of *ab initio* calculations (Ref. 33).

In a communication to this journal[1] we have reported on our approach to this problem, to reach the TS directly through a CT excitation of a bimolecular van der Waals (vdW) complex of A and BC using femtosecond (fs) laser pulses. The fs pulse (denoted by solid arrow in Fig. 1) prepares the TS, $[A^+\cdots{}^-BC]^{*\ddagger}$, from a well-defined ground-state TS, $[A\cdots BC]^{\ddagger}$, at known intermolecular separations and geometry. The dynamics is then followed by monitoring the TS or the reaction products by using probe fs pulses, with a mass spectrometry arrangement in the molecular beam apparatus. The advantage of using a vdW complex as the reaction precursor in the fs real-time studies is twofold:[2,3] (1) the zero-of-time of the reaction is precisely defined and (2) the impact geometry is defined by the structure of the vdW complex. These bimolecular CT reactions are unique among the different classes of CT reactions studied on the fs and ps time scales, which include unimolecular harpooning reactions,[4] intramolecular CT reactions,[5] proton transfer in acid–base reactions,[6] harpooning reactions of $Xe+I_2$ (Ref. 7) and, more recently, $Xe+Cl_2$.[8] The specific system of interest here is the bimolecular reaction of polyatomic molecules (electron donor, D) benzene (Bz), or methyl substituted benzenes (MBz) with a diatomic molecule (electron acceptor, A) of molecular iodine (I_2); see Fig. 2. The system is rich in many aspects of structure and dynamics and has been extensively studied for nearly 50 years since the seminal works by Hildebrand[9] and Mulliken.[10,11]

The concept of the experiment is illustrated in Fig. 3 by considering the two nuclear coordinates, the Bz–I and I–I distances. If the $t=0$ pulse is at the vdW distance ($\lambda^{\ddagger}$), then the TS is reached by direct CT, for a given geometry, followed by bond breakage along the I–I coordinate. On the other hand, if the $t=0$ pulse (λ^{∞}) is tuned to one of the reactants, then the situation is equivalent to a bimolecular collision with full impact parameter sampling; in this case the crossing of the covalent to the ionic curve is crucial to the outcome. Vertical excitation from the vdW geometry to the CT state induces a fs electron jump from benzene to iodine and suddenly turns on the Coulomb field between the two. The iodine molecular anion is then rapidly pulled in by the strong electrostatic force to a closer distance from the benzene cation and then the reaction occurs. The products are a free iodine atom and a $Bz^+\cdot I^-$ complex. While in the TS, an electron may return back to benzene and the covalent exit channel (BzI+I) opens up. By monitoring the decay of the TS, the appearance of the free I atoms, and their kinetic energies, we are able to directly observe the evolution of the TS from a well-defined structure. By measuring the vectorial correlation between the direction of recoil and the initial alignment we obtain the (impact) geometry at $t=0$ for the TS.

Comparisons with other (time-integrated) approaches are relevant. In Polanyi's TS spectroscopy of the $Na+XCH_3$ system,[12] they reach the covalent branch and then by crossing, through harpooning, the final products are made. The scheme in Fig. 1 is similar to that of the $M+X_2$ harpoon reactions, where M=alkali–metal atom and X=halogen

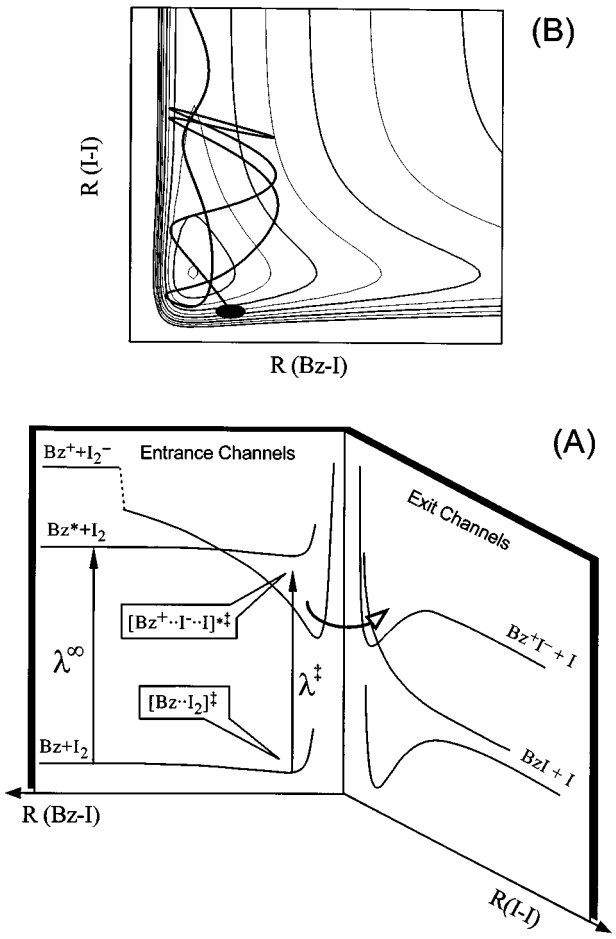

FIG. 3. (A) A schematic diagram showing the cuts on the PES along the Bz–I and I–I coordinates. In the present study, the CT transition state is directly reached by the $t=0$ fs pulse ($\lambda^\ddagger$). The reaction proceeds through the exit channels either on the same CT PES shown in (B) or through nonadiabatic transitions which leads to the I–I bond breakage. (B) A PES contour map of the $Bz \cdot I_2$ CT state and a representative trajectory of the reaction on this PES (see the text).

atom, except that the present system requires a photon to induce the electron jump and enters the transition-state region directly. The preparation is from ''beneath'' the potentials of interest and in this regard analogous to Neumark's[13] photodetachment experiments. The preparation is off-resonant with the absorption of either reactants, similar in design to Brooks's[5] and Curl's experiments.[14] The mechanism also bears a close similarity to that in reactions of $Xe \cdot X_2$ (X=Cl, Br)[15] and $Hg \cdot Cl_2$ complexes reported by Jouvet and Soep,[16] and the laser-assisted reactions of Xe/X_2 collision pairs reported by Setser's group.[17] In these cases, the vdW complexes (or collision pairs) were excited to their CT states by one or two photons and the product's (XeX* and HgCl*) emission was detected. Finally, unlike the hot-atom reactions,[2,18] the $Bz \cdot I_2$ system is entirely prepared on a reactive potential at $t=0$ and has a well-defined impact geometry, as discussed below, and in this sense is a prototype for both Polanyi's surface-aligned reactions[19,20] and dissociative reactions at electrodes as described by Savéant,[21] Eberson,[22] and others.

In this paper, we give a full account of our work reported in the earlier communication.[1] Although donor–acceptor complexes of benzene with I_2 have been extensively studied for nearly a half century, very little is known about the nature of the TS state and its dynamics. The present study is aimed at elucidating the dynamics of the 1:1 complex following the CT excitation in a collisionless environment free of solvent perturbations. Elsewhere, we described the effect of further solvation with benzene.[23] Because the complexes were prepared in a supersonic molecular beam, the internal temperatures of the complexes are very low (~10 K). The conditions were carefully adjusted to ensure the dominance of 1:1 complexes in the molecular beam. The energetics of the TS were varied by changing the initial pulse wavelength. Geometry (impact parameter) and symmetry considerations were examined by studying the following donor aromatics: D=benzene, deutrobenzene, toluene, and also xylenes and trimethylbenzenes of different symmetries. We employed the fs time-resolved kinetic energy time-of-flight and anisotropy measurements to reveal the product translational energy distributions and the nature of the two distinct channels involving the neutral and ionic potentials. Theoretical studies involving *ab initio* calculations and molecular dynamics are also reported.

The paper is outlined as follows. In Sec. II, we briefly discuss spectroscopic and theoretical studies and the current understanding of CT with a special focus on the $D \cdot I_2$ system. In Sec. III, the experimental techniques and methodology are described, including the femtosecond laser system, molecular beam apparatus, time-of-flight mass spectrometer (TOF-MS), and the kinetic energy resolved TOF-MS. In Sec. IV, the experimental results are presented. In Sec. V, we discuss the experimental results and provide the dynamical picture and reaction mechanism.

II. THE CT SYSTEM

It has been recognized for more than a century that different colors develop when iodine is dissolved in a variety of solvents.[24] Organic solvents were in those days distinguished based on the colors of their iodine solutions since, in general, saturated solvents gave a violet color and unsaturated ones gave a brown color. In 1949, in an attempt to reveal the origin of this phenomena, Benesi and Hildebrand[9] discovered a strong UV absorption band that is characteristic of neither the aromatic solvents nor the iodine molecules alone. They attributed these new absorption bands to the formation of aromatic-I_2 ($D \cdot I_2$) complexes and proposed that they are stabilized by ''acid–base'' interactions in solutions. Soon after this discovery, Mulliken[10,11] developed a theory to account for the stability and the strong UV absorption of $D \cdot I_2$ complexes. He proposed that the complex is stabilized by resonance interactions between a ''no-bond'' ($D–I_2$) and a ''dative-bond'' ($D^+ - I_2^-$) CT structures, in which the aromatic molecule acts as an electron donor and I_2 the electron acceptor. The new absorption band is then simply due to the excitation of the ground state complex to the CT state.

Based on Mulliken's theory, the CT absorption band en-

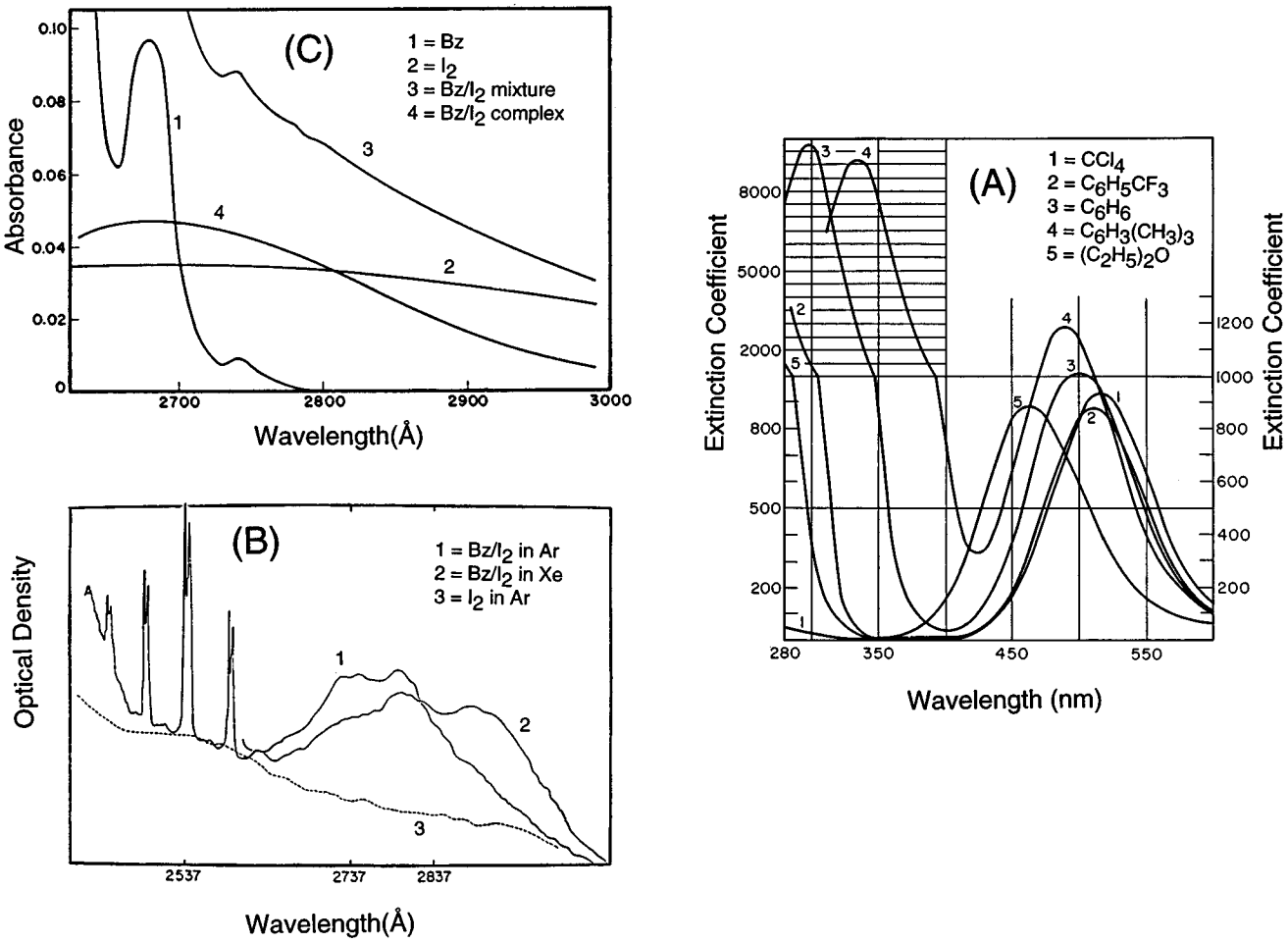

FIG. 4. (A) Absorption spectra of iodine solutions with various solvents. The absorption in the visible region is due to the uncomplexed I_2 $B \leftarrow X$ band, whereas that in the UV region is due to the complex CT absorption. Note the different scales in the two regions and the very weak absorption when iodine is dissolved in the ''inert solvent'' CCl_4. The figure is adopted from Ref. 9. (B) Absorption spectra of $Bz \cdot I_2$ in Ar and Xe solid matrices at 20 K. The broad absorption bands centered around 281 nm (Ar) and 285 nm (Xe) are due to the $Bz \cdot I_2$ CT absorption. The sharp features in the $\lambda \leqslant 260$ nm region are due to the uncomplexed benzene $S_1 \leftarrow S_0$ absorption. Note that when only I_2 was deposited in the matrix no CT absorption was observed (the dashed line). Adopted from Ref. 28. (C) UV absorption spectra of gas phase benzene, iodine, and Bz/I_2 mixtures at a temperature of 340 K. The $Bz \cdot I_2$ complex absorption spectrum was obtained from the difference. The concentration of the $Bz \cdot I_2$ complex was estimated to be 2–3 orders of magnitude smaller than those of uncomplexed I_2 and Bz in the gas mixture. Adopted from Ref. 29.

ergy can be approximated by the following equality:

$$h\nu_{CT} = IP(D) - EA(A) - W, \tag{3}$$

where IP(D) is the ionization potential of the electron donor, EA(A) is the electron affinity of the electron acceptor, and W is the Coulomb interaction energy (e^2/R). Many experiments were followed to test Mulliken's theory. However, it was soon clear, based on experimental evidence as well as theoretical arguments,[25] that the contribution of the CT state to the ground state stability is small. Nevertheless, spectroscopic studies of a variety of electron donor/acceptor systems have in many cases confirmed the correlation of the CT band energy with the IP and EA.[11,26,27] It is now generally accepted that the strong characteristic UV absorption bands of $D \cdot I_2$ and other related complexes are due to the CT excitation. However, the ground state complexes are bound simply by the dispersion force and electrostatic multipole interactions.

Benzene$\cdot I_2$ ($Bz \cdot I_2$) and other similar complexes are probably the most well studied CT complexes.[26,27] Various conventional spectroscopic methods have been employed to investigate these complexes in the liquid, gas, and solid phases. In Fig. 4(a) representative absorption spectra reproduced from the literature show the original ultraviolet–visible absorption reported by Benesi and Hildebrand[9] for several I_2/D solutions. The CT absorption band maximum of the I_2/Bz solution is at 297 nm. Note the much smaller extinction coefficient in the UV region when I_2 is dissolved in an ''inert solvent'' such as CCl_4. Figure 4(b) shows clear absorption spectra of $Bz \cdot I_2$ isolated in Ar and Xe solid matrices at 20 K.[28] The center of the absorption band in the Ar matrix is around 281 nm. Figure 4(c) shows gas-phase absorption spectra of a Bz/I_2 vapor mixture at 340 K.[29] The CT absorption maximum shifts to 268 nm in the gas phase. Similar CT absorption bands of many I_2/D systems have been

observed and widely studied. In general, the positions of the CT absorption maxima exhibit a strong correlation with the IPs of the electron donors and qualitatively agree with the prediction made by Eq. (3).[11,26,27]

The $D \cdot I_2$ complexes are known to be stable even in room temperature solutions. The heat of complex formation of $Bz \cdot I_2$ in the gas phase has been determined by spectrometric methods to be on the order of -2 to -3 kcal/mol.[29,30] A more recent molecular beam experiment[31] has reported the binding energy of $Bz \cdot I_2$ to be 745 ± 70 cm^{-1}. An early *ab initio* study[32] has predicted a binding energy of about 700 cm^{-1} for $Bz \cdot I_2$. As discussed below, our *ab initio* calculations[33] of the 1:1 complex give a similar binding energy.

Mulliken[10] initially suggested that $Bz \cdot I_2$ has a ''resting'' structure, with the I–I bond lying above and parallel to the benzene molecular plane. However, IR spectroscopic studies[34] of Bz/halogen solutions suggest an axial structure similar to the one shown in Fig. 2. In this structure, the I–I axis is along the benzene C_6 axis and the complex has a C_{6v} symmetry. X-ray studies of two very similar systems, namely $Bz \cdot Br_2$ and $Bz \cdot Cl_2$,[35] in their 1:1 crystal forms have also shown results that are consistent with the axial structure. UV and IR spectroscopic studies of $Bz \cdot I_2$ in solid matrices have also concluded that the complex has an axial structure.[36] Several theoretical studies,[32,33,37] including *ab initio* calculations,[32,33] have predicted that the axial structure is indeed the most stable form of the $Bz \cdot I_2$ complex. The experimental results mentioned above, although favoring the axial structure, do not address the structure of the isolated 1:1 $Bz \cdot I_2$ complex derived from experimental studies of the isolated species.

Photochemistry of $D \cdot I_2$ complexes was also a subject of interest for many years. Microsecond flash photolysis studies of I_2/D solutions[38] and vapor mixtures[39] have reported transient visible absorption bands that can be assigned to D–iodine atom (D·I) complexes. The first ultrafast picosecond (ps) laser studies[40] found that D·I complexes are formed very rapidly in I_2/D solutions upon I_2 and CT excitation. The time resolution was not sufficient to resolve the initial dynamics. With the advent of fs laser spectroscopy, the photochemistry of $D \cdot I_2$ complexes has attracted new interest. Fs laser studies[41–44] have been reported recently and shown that the formation of D·I complexes is indeed extremely fast (25–500 fs) upon CT excitation of I_2/D solutions. We will review and compare results of the liquid-phase fs studies with our gas-phase and cluster results in Sec. V.

III. EXPERIMENT AND METHODOLOGY

A. Femtosecond laser systems

Two fs laser systems were used here, the colliding pulse mode-locked ring dye laser (CPM) and the synchronously pumped dye laser, both with amplifiers. The CPM system has been described elsewhere[45] and here we only describe the synch-pumped laser system. The CPM system was used for its high time resolution (~60 fs) while the synch-pumped system provided versatility in tunability and in the resonance

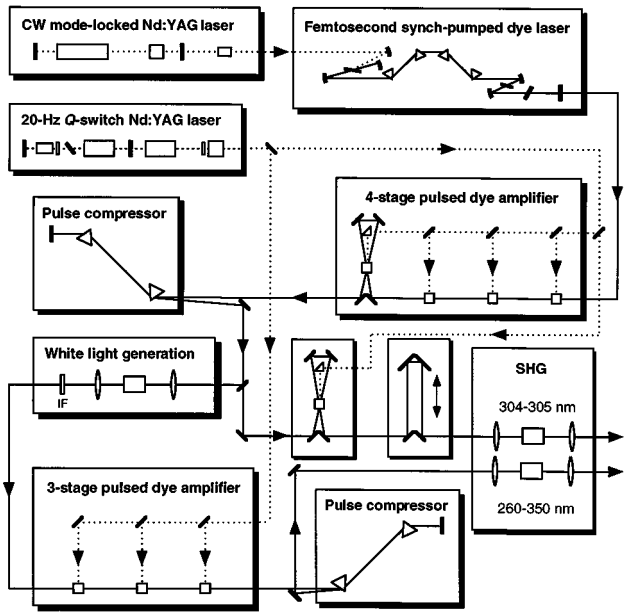

FIG. 5. Schematic layout of the synch-pumped femtosecond laser system. See the text for detail.

detection of the iodine atom. The CPM system with the molecular beam[46] was specifically used to measure the ultrafast decay of the TS and the synch-pump systems was used for all other experiments.

The synch-pumped laser system employed here is schematically shown in Fig. 5. The second-harmonic output of a 76 MHz mode-locked Nd:YAG laser (Coherent Antares 76S) was used to synchronously pump an ultrafast dye laser (Coherent Satori) to generate fs laser pulses. The dye laser is of the hybrid mode locking linear cavity design, employing twin jets, and dispersion compensated by a prism pair. Solutions of Rhodamine 610 and DODCI laser dyes (exciton) in ethylene glycol were used as the gain medium and the saturable absorber, respectively, to produce laser radiation around 610 nm. The mode locking of the dye laser was continuously monitored by a homemade real-time scanning autocorrelator. Typical characteristics of the dye laser output pulses are 200 fs full width at half maximum (FWHM) and 2 nJ/pulse.

The resulting fs laser pulses were amplified through a four-stage pulse dye amplifier pumped by the second-harmonic output of a 20 Hz Q-switch Nd:YAG laser (Spectra-Physics DCR-2A). The first three stages were side-pumped and employed SR-640/water as the gain media. The last stage was end-pumped and used R640/water as the gain medium. The amplified pulses (~400 μJ/pulse) were then recompressed through a SF-10 prism pair to compensate for the group velocity dispersion occurring during the amplification. To generate pump pulses between 260 and 290 nm, 80% of the amplified 610 nm beam was split off by a beam-splitter and was focused into a small quartz cell containing D_2O to generate a white light continuum. Different spectral portions of the continuum were selected by interference filters (10 nm FWHM) centered at the desired wavelengths.

The filtered continuum was reamplified in a three-stage dye amplifier pumped by the second- or third-harmonic output of the same Q-switch Nd:YAG laser used to pump the first dye amplifier. The resulting pulses were then frequency doubled through a 0.5 mm KDP crystal to produce the pump pulses ($\sim$5–10 μJ/pulse).

The remaining 20% of the 610 nm light was amplified again through a single-stage dye amplifier (R640/water) with a double-pass arrangement. The resulting pulses were delayed in time by a retroreflector mounted on a computer controlled translation stage (Dynaoptic Motion), and then frequency doubled by a 0.5 mm KDP crystal to obtain the probe pulses at around 304 nm ($\sim$20 μJ/pulse) for 2+1 resonance-enhanced multiphoton ionization (REMPI) detection of free iodine atoms. The pump and probe beams were recombined collinearly by a dichroric beamsplitter and were focused and spatially overlapped in the extraction region of a time-of-flight mass spectrometer (TOF-MS). Time-resolved transients were obtained by monitoring the ion signal of certain mass channel using a boxcar integrator while the pump–probe delay time was scanned. The transients reported here are typically the average of 20–100 scans. For most of the transients reported here, the pump laser polarization was parallel to the TOF-MS axis and orthogonal to the probe laser polarization. In some experiments, the pump laser polarization was rotated by a half-wave plate prior to frequency doubling.

The free iodine atoms produced in the reactions were ionized through 2+1 REMPI. Several two-photon allowed atomic transitions originating from the ground state of iodine atom $^2P_{2/3}$ (I, 304.67, 304.55, and 303.69 nm) and the spin–orbit excited state $^2P_{1/2}$ (I*, 305.57, and 304.02 nm) have been reported to lie in the general spectral region of the probe laser. The bandwidth of the probe laser ($\sim$2 nm) therefore allows simultaneous detection of both I and I* (see the Appendix). Because of the resonance detection through narrow atomic transitions, the I^+ intensity is very sensitive to the probe wavelength. To ensure resonance detection, the output wavelength of the dye laser was carefully tuned by adjusting a birefrigent filter placed in the dye laser cavity and was measured by a calibrated monochrometer. For the experiments reported here, the dye laser wavelength was tuned to 609.0$\pm$1.0 nm. All dye solutions used in the dye amplifiers were kept at the lowest concentrations possible to minimize spectral broadening and distortion. The probe pulses produced in this manner are centered at about 304.5 nm and have a bandwidth of $\sim$2 nm. For probing the $Bz\cdot I_2$ CT state we used either the 609 or 304 nm for ionization.

The zero-of-time and the cross correlation of the pump and probe pulses were determined by measuring the transient rise of the aniline 1+1 REMPI signal through its S_1 state. These diagnostic experiments were performed in a small ionization cell located near the entrance window of the molecular beam apparatus. The S_1 state of aniline is very long lived (7.9 ns), therefore the 1+1 REMPI transient rise is equivalent to the convolution of the pump–probe correlation with a step function on the time scales of interest. The typical pump–probe cross correlations were 500$\pm$50 fs FWHM for the synch-pumped laser system, and $\sim$140 fs for the CPM. The zero-of-time was also calibrated from *in situ* experiments in the molecular beam done on the very weak iodine atom signal produced from the uncomplexed molecular iodine, as discussed below.

B. Molecular beam apparatus

The experiments were carried out in a conventional two-chamber molecular beam apparatus schematically shown in Fig. 6(A). Briefly, a supersonic molecular beam containing the species of interest was produced in the first chamber, skimmed, and intersected by the fs laser beams in the extraction region of a two-stage linear TOF-MS housed in the second chamber. The ions were detected by a 25-mm-diam microchannel plate assembly (MCP). The molecular beam, TOF-MS axis, and the fs laser beams were orthogonal to each other. A pair of deflection plates was used in the field free region to correct for the drift of ion trajectories due to the molecular beam velocity component perpendicular to the TOF axis. The TOF-MS was also used as a kinetic energy spectrometer, as described in Sec. III C, to resolve the translational energy distribution of reaction products.

The $D\cdot I_2$ complexes were produced by expanding gas mixtures containing donor aromatics, iodine, and He through a pulsed valve (General Valve Series 9) with an orifice of 0.5 mm in diameter. The gas mixtures were prepared by allowing pure He gas (800–1000 Torr) to flow, first through a reservoir containing electron donors, and then over iodine crystals loosely packed in a Teflon tube. This ensured complete mixing of gases before expansion. The iodine crystals were kept at room temperature ($\sim$22 °C). The donor reservoir was immersed in a large cold bath. The concentration of the donor vapor in the gas mixture was adjusted by varying the cold bath temperature which was carefully monitored and controlled during the experiments. All electron donors studied in this work were used as purchased (Aldrich, >98%).

As expected, because of the relatively large polarizabilities of the D's and I_2, they cluster very easily in the jet. Since only the iodine atom products were monitored, it is very important to control and diagnose the cluster size distribution in the beam. This was achieved by controlling the donor vapor concentration in the gas mixtures. We used the pump laser (277 nm) alone as the ionization laser to monitor the cluster size distribution. Figure 7(A) shows a series of mass spectra taken at different benzene concentrations with all other conditions fixed. We believe that these spectra reflect the true beam composition because the complexes were ionized at a total energy not much higher than their IPs. Under our beam conditions, the benzene concentrations needed to be as low as 0.5 Torr to avoid any appreciable amount of $n \geqslant 2$ clusters. At higher benzene concentrations, larger clusters were clearly present in the beam. Similar behaviors were observed for all D/I_2 systems studied here. The results presented in this work, except those in Fig. 7(B), are all obtained under the 1:1 complex condition.

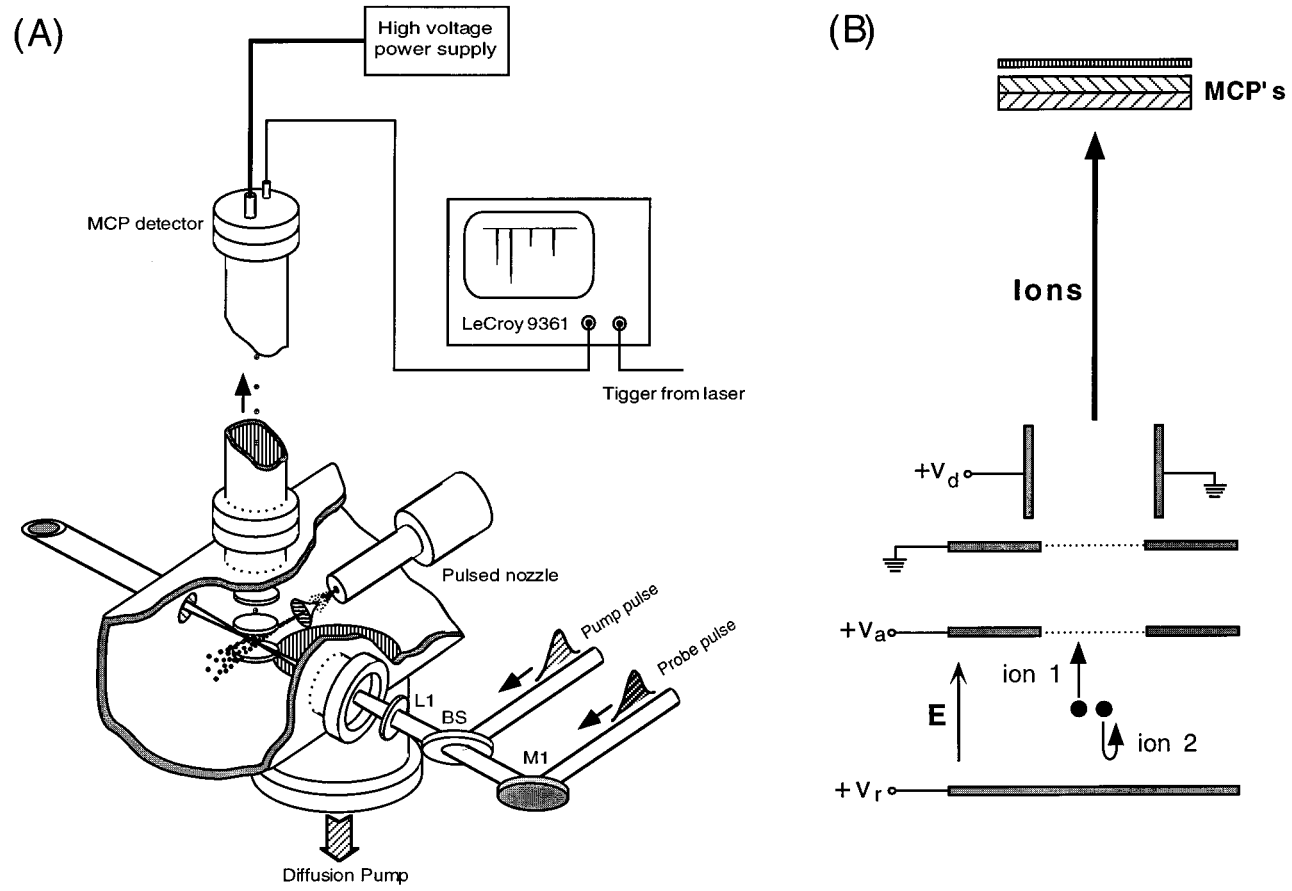

FIG. 6. (A) Schematic representation of the molecular beam apparatus. The pulsed nozzle and the TOF-MS are located in two separated chambers connected by a skimmer. (B) Schematic diagram showing the ''turn-around time'' for two ions (1 and 2) initially moving parallel to the TOF-MS axis with the same speed but in opposite directions (see the text).

C. Fs time-resolved kinetic energy spectrometer: Fundamentals and techniques

The use of a TOF-MS as a kinetic-energy spectrometer has been described by many authors.[47–51] ''Kinetic-energy resolved TOF-MS,'' or KETOF is a powerful addition to dynamical studies on the fs time scale. This group[52–54] has recently combined fs techniques with KETOF in several cases to separate different reaction channels. A full discussion of the KETOF experiment and data analysis is presented in the Appendix. Here, we only briefly mention the fundamental ideas and the experimental details.

Suppose that a pump laser pulse comes in and produces two fragments of the same mass recoiling with the same speed along the TOF axis (z) but in opposite directions, as schematically shown in Fig. 6(B). After a short time delay, a probe pulse comes in and ionizes both fragments. The one going toward the detector (ion 1) is accelerated by the extraction field and arrives at the detector after its time-of-flight. The one that is initially going away from the detector (ion 2) is decelerated by the extraction field, reaches a complete stop, and is then accelerated again back to its initial position. Thereafter, ''ion 2'' follows exactly the same trajectory as ''ion 1.'' Hence, the arrival time of ion 2 is delayed from that of ion 1 by the ''turn-around time,'' which can be shown to be

$$\Delta t = 2m|v_z|/qE, \tag{4}$$

where m and q are the mass and charge of the ionized fragments, E is the extraction electric field strength, and v_z is the projection of the recoil velocity on the TOF axis (z). Since the turn-around time is linearly proportional to $|v_z|$, the velocity distribution of the fragments causes a spread in the arrival time around the $v_z=0$ fragments. The observed KETOF distribution is therefore a one-dimensional projection of the three-dimensional recoil velocity distribution onto the TOF axis.

Ideally, the observed KETOF distribution can be directly transformed into v_z distribution, as described in the Appendix. Practically, it is complicated by the fact that TOF also depends on the position where the dissociation occurs along the z axis. This problem was minimized in our experiments by operating the TOF-MS under near space-focusing conditions and by focusing the laser beam to small spot sizes. The initial thermal distribution of the parent molecules is negligible under the skimmed supersonic beam conditions. The major limiting factor to the energy resolution is the space-

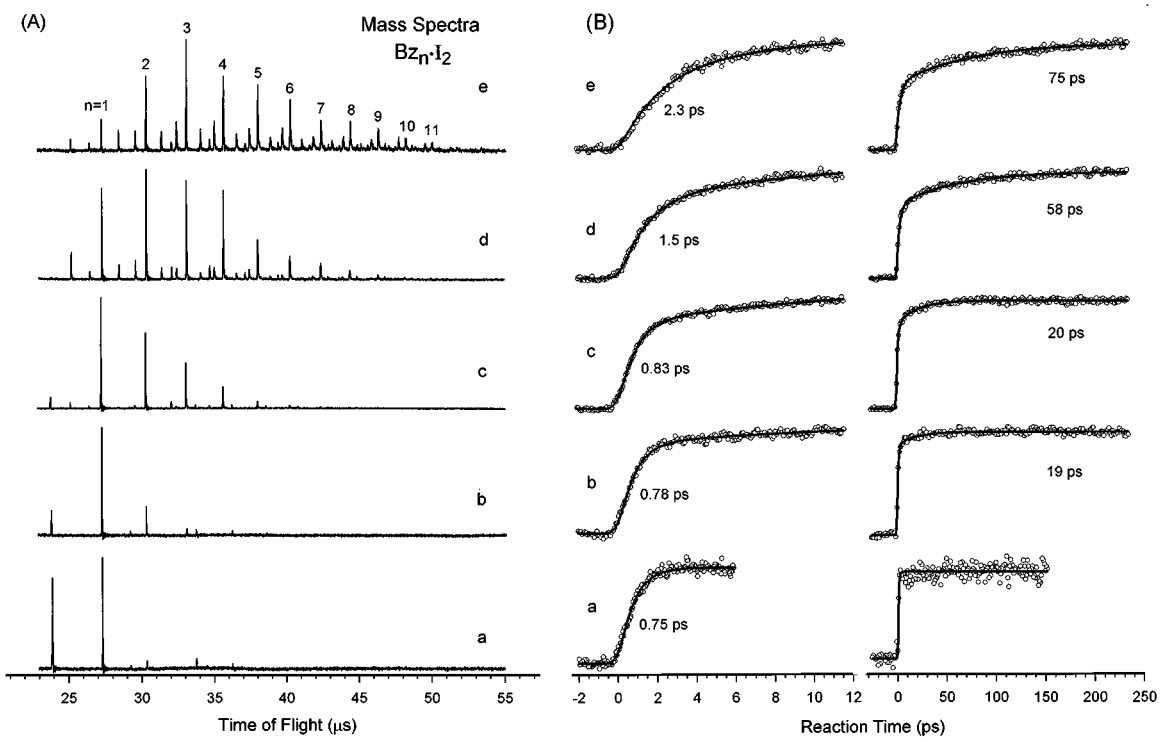

FIG. 7. (A) TOF-MS spectra taken under identical conditions except with different benzene vapor pressures in the gas mixtures: (a) 0.5 Torr; (b) 1.3 Torr; (c) 3.3 Torr; (d) 9.5 Torr, and (e) 24 Torr. These spectra were obtained by using the 277 nm fs pulses alone as the ionization laser. The laser intensity was reduced to minimize fragmentation of cluster ions. The TOF-MS parameters were optimized for the general mass range of $n=4$–6 clusters. (B) Free iodine atom transients obtained under the corresponding conditions in (A). The transients displayed in the right-hand panel show the long-time behavior while those displayed in the left-hand panel show the early time dynamics. The open circles are the raw data and the solid lines are the results of biexponential rise fits. The time constants for the slower components were obtained by fitting the long-time transients. The time constants for the faster component were then obtained by fitting the short-time transients with the slow component time constants fixed. All transients were normalized to the same maximum for comparison. The absolute transient iodine atom signal actually increases with the benzene concentration.

charge effect, which was minimized in our experiments by reducing the laser intensities until no significant change was observed.

In our previous report[1] of the preliminary results of this work, we used a ~110-cm-long TOF-MS flight tube and a relatively low acceleration voltage. These resulted in a I^+ TOF of ~23 μs which discriminated against high velocity fragments, because ions with a high velocity component ($\geqslant$550 m/s) perpendicular to the TOF axis cannot be detected. This discrimination effect, if properly utilized, can be very useful in resolving different velocity components.[48] However, in experiments where knowledge of the relative ratios of different velocity components is crucial, this approach is not suitable.

We have taken a different approach in the present work. First, we shortened the I^+ TOF to ~7.2 μs by using a shorter TOF-MS flight tube (~45 cm) and a higher acceleration voltage while keeping the extraction electric field at a low level. These ensure that we collect all the ions and still have a good kinetic energy dispersion. Second, the KETOF distributions were measured with the pump laser polarization oriented at the ''*magic angle*'' (54.7°) with respect to the TOF-MS axis. Under this condition, the KETOF distribution observed is independent of the recoil anisotropy (β), as discussed in the appendix, and hence the recoil speed distribution can be extracted. KETOF distributions were also measured with the pump laser polarization *parallel* or *perpendicular* to the TOF-MS axis in order to obtain the anisotropy distribution β(v). We will discuss these procedures in more details in the appendix.

The electric field strength in the extraction region was kept at ~65 V/cm for all KETOF experiments except in cases where trimethylbenzenes were the donors. In such cases, the field strength was increased to ~200 V/cm to avoid overlapping of the much greater ion signal at the donor mass channel with the iodine atom KETOF distribution. The KETOF distributions were measured by recording the TOF distributions of I^+ at a fixed pump–probe delay time using a digital storage oscilloscope (LeCroy 9361, 300 MHz). The time-independent background of the I^+ TOF distribution produced by the pump and probe lasers alone were separately recorded and subtracted from the pump+probe distributions. Both the total and the background signals were averaged for the same number of laser shots, typically 10 000. For time-resolved KETOF studies, the same procedure was repeated for a series of pump–probe delay times controlled by the translation stage.

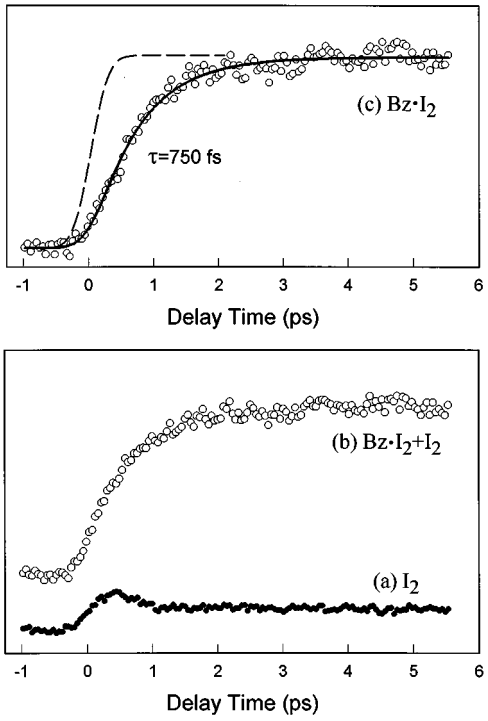

FIG. 8. (a) Background iodine atom transient obtained when only I_2 is present in the gas mixture. (b) Iodine atom transient recorded when both I_2 and benzene are present in the gas mixture. The benzene vapor pressure is ~0.5 Torr, i.e., the 1:1 condition. (c) Result of subtraction of transient (a) from transient (b). The open circles are the raw data and the solid line is a single exponential fit. The dashed line is an aniline 1+1 REMPI transient resembling the system response. Note the similarity between transient (b) and (c).

IV. RESULTS AND ANALYSES

A. The $Bz \cdot I_2$ complex: Characterization and preparation

Free iodine atoms were readily detected by the probe laser when $Bz \cdot I_2$ complexes were excited to their CT absorption band region in the molecular beam. The iodine atom transient, i.e., the trace representing the iodine atom signal as a function of pump–probe delay time, depends strongly on the benzene vapor concentration in the expanding gas mixture, as shown in Fig. 7(B). At high benzene concentrations, the transients are characterized by biexponential rises, with the slower component being 20–75 ps, depending on the benzene concentration.[23] As the benzene concentration is reduced, the ratio of the slow to fast component decreases. At the lowest benzene concentration [0.5 Torr, (a) in Fig. 7], the long-time component essentially vanishes, and the iodine atom signal stays at a constant level for more than 200 ps. However, at this low benzene concentration, the density of the complexes also becomes so low that the background I^+ signal arising from the much more populated uncomplexed molecular iodine in the beam becomes significant. Figure 8(b) shows an early time transient taken under this very low benzene concentration condition. A background iodine atom transient shown in Fig. 8(a) was recorded right after[55] the Fig. 8(b) transient was taken but with He gas bypassing the benzene reservoir, i.e., no benzene in the gas mixture. Figure 8(c) is a corrected transient obtained by subtracting Fig. 8(a) from Fig. 8(b). As also shown in Fig. 8, the rise of the corrected transient is clearly slower than the response function and can be described by an apparent single-exponential rise of 750±50 fs (see below).

The build up of free iodine atoms produced by the 1:1 $Bz \cdot I_2$ CT state reaction was established based on the following. First, this transient iodine atom signal can be observed *only* when benzene and iodine vapors are both present in the expanding gas mixture. As manifested in Fig. 8, when pure iodine vapor is expanded with He gas alone, only a much weaker iodine atom background can be observed [see Fig. 4(A) for solution phase work]. These observations indicate that the transient iodine atom signal must arise from complexes associated with both Bz and I_2. The weak iodine background transient may involve a very weak absorption of I_2 as well as I_4 in the pump laser wavelength region, as discussed by Mulliken.[56] Contributions due to multiphoton absorption of I_2 are also possible. Second, as shown in Fig. 7, the change of the iodine atom transients is unequivocally associated with a dramatic evolution in the mass spectra as the benzene vapor concentrations were varied. At high benzene concentrations, large-sized clusters dominate the beam composition, whereas the $Bz \cdot I_2$ 1:1 complex is the only one detectable at the lowest (0.5 Torr) benzene concentration. Further lowering of the benzene concentration decreases the transient iodine atom signal, but does not change the shape (rise time constant) of the transients. Based on these observations, we conclude that the transients observed at the lowest (0.5 Torr) benzene concentration are due to the *1:1 $Bz \cdot I_2$ complex*. The transients observed at higher benzene concentrations have been discussed elsewhere on the basis of the caging dynamics in larger clusters.[23]

Further support comes from the initial preparation. The pump laser wavelength (260–285 nm) used here is near the reported CT absorption maxima of the complex (see Fig. 4).[9,28,29] The CT band of the $Bz \cdot I_2$ complex is well known for its strong absorption due to the inherent CT nature of the transition described by Mulliken's theory.[10,11] The uncomplexed I_2, on the other hand, absorbs very weakly in this spectral region.[56] Gas phase studies[29] have shown that the extinction coefficient of the $Bz \cdot I_2$ complex is at least 150 times larger than that of the free I_2 in the pump laser wavelength region. This strong CT absorption is consistent with our observation that many more I atoms are produced from the $Bz \cdot I_2$ complexes, even though their concentration is expected to be only a few percent of the uncomplexed I_2 in the molecular beam. Moreover, the lowest pump laser photon energy employed here is about 3000 cm^{-1} lower than the free benzene $S_1 \leftarrow S_0$ band origin. For many mixed bimolecular complexes containing benzene, the spectral shifts of the benzene $S_1 \leftarrow S_0$ transition are usually smaller than ±200 cm^{-1}.[57] Therefore, excitation through the local benzene $S_1 \leftarrow S_0$ transition is not possible, but instead, the *initial excitation must reach the $Bz \cdot I_2$ CT state*.

At higher benzene concentrations the $(Bz)_n \cdot I_2$ complexes can be ionized by the pump laser alone through 1+1

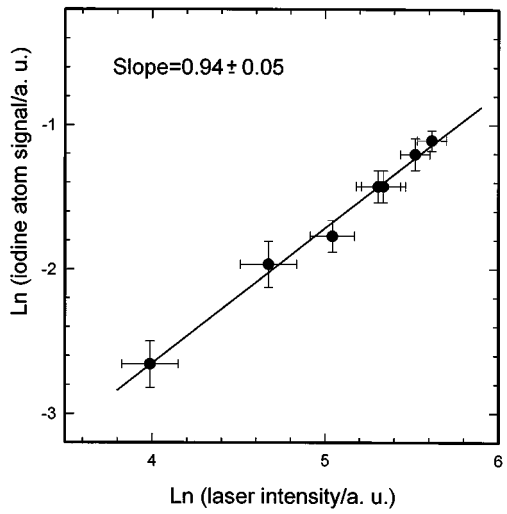

FIG. 9. Pump laser (277 nm) intensity dependence of the transient iodine-atom signal measured at a pump–probe delay time of ~1 ps. These measurements were carried out under the ''cluster condition'' as the signal level under the 1:1 condition is too low to be measured accurately with reduced laser intensity. However, at 1 ps the contribution from the larger clusters is minimal. Moreover, the pump laser intensity dependence measured at a very long delay time of ~500 ps gave essentially the same result, indicating that the iodine atoms are produced at a one-photon excitation level for both the 1:1 and larger complexes. The slope is 0.94±0.05.

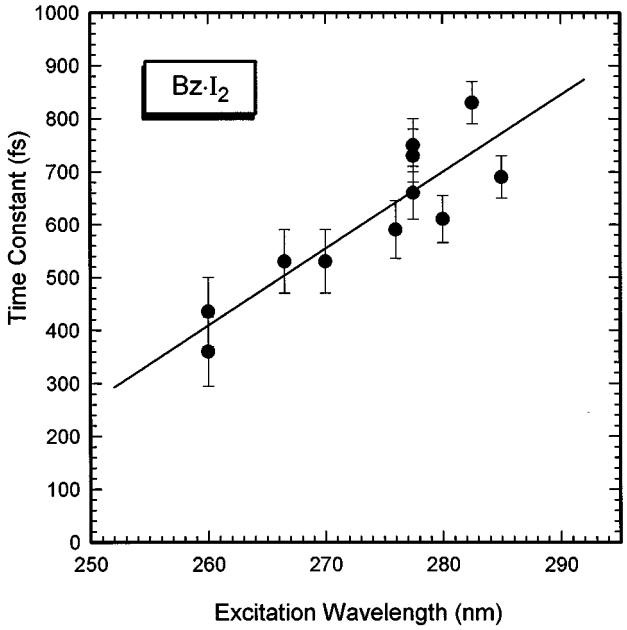

FIG. 10. Pump laser wavelength dependence of the apparent rise time constants of the iodine transient observed for the $Bz \cdot I_2$ reaction. Each data point (●) represents the result of a single run of experiment. The solid straight line is only for guidance of the trend.

REMPI, as shown in Fig. 7(A). If reactions occur in the complex's cation, which may also produce neutral iodine atoms, transient rises of the iodine atom signal could be observed. To clarify this possibility, we have performed diagnostic experiments to measure the pump laser intensity dependence of the transient iodine atom signal. The results are shown in Fig. 9. The power dependence of the pump laser was found to be approximately linear, indicating the transient iodine atom signal observed was produced at a one-photon excitation level. This is further supported by observations that the iodine atom transients were eventually unchanged when the pump laser intensity was reduced by nearly a factor of 10.

The iodine transients were also measured at several different pump laser wavelengths between 260 and 285 nm in order to elucidate the initial energy dependence. The results are shown in Fig. 10, in which the measured rise time constants are plotted against the pump laser wavelength. Clearly, the apparent rise becomes faster as the excitation energy increases.

B. Other $D \cdot I_2$ complexes: Tuning the CT and changing the structure

To understand the dependence of the reaction dynamics on the nature of the electron donor, we have studied similar I_2 complexes with six methyl-substituted benzenes (MBz) and deutrobenzene (d_6) at λ_{pu}277 nm. Figure 11 shows representative iodine atom transients resulting from the reactions of $C_6D_6 \cdot I_2$, toluene$\cdot I_2$, m-xylene$\cdot I_2$, and 1,2,4-trimethylbenzene$\cdot I_2$. The apparent rise time constants are all in the range of 0.6–1.0 ps. Note that in the $C_6D_6 \cdot I_2$ case, the time constant is very close to that of $Bz \cdot I_2$. The other two xylene isomers also give similar rise time constants as the o-xylene, and mesitylene$\cdot I_2$ gives about 1.0 ps. Except for toluene$\cdot I_2$, the rise time increases as the number of methyl groups on the benzene ring increases.

The CT absorption bands of these $MBz \cdot I_2$ are expected to be lower in energy than that of $Bz \cdot I_2$ because of the lowering in IPs of the donors. For example, the gas phase CT band maximum of mesitylene$\cdot I_2$ is at ~301 nm,[58] about 0.5 eV lower than the $Bz \cdot I_2$ maximum. Hence, our excitation energy (277 nm) falls at the blue side of the $MBz \cdot I_2$ CT absorption bands.

The S_1 states of MBz are also lower in energy than $Bz(S_1)$.[59] Some MBz have S_1 zero-point energies close to or even below our excitation energy. Excitation to the MBz locally excited states is therefore possible. However, the CT transition is much stronger than the aromatic $S_1 \leftarrow S_0$ local excitations, making the contribution of the locally excited S_1 state small. This is consistent with the following: (1) in the xylene$\cdot I_2$ and mesitylene$\cdot I_2$ cases, we have tuned the photon energy down to ~290 nm and observed no significant changes in the rise times; (2) no drastic dynamical change was observed in going from $Bz \cdot I_2$ to trimethylbenzene$\cdot I_2$; and (3) the $S_1 \leftarrow S_0$ transition dipoles in MBz are polarized in the molecular plane which is inconsistent with the conclusion we will reach later regarding the recoil anisotropy. As mentioned before, for $Bz \cdot I_2$, we only reach the CT state because the $S_1 \leftarrow S_0$ of benzene is at higher energy.

C. KETOF: Translational energy distributions

The translational energy distributions of iodine atoms produced from the CT reactions bear detailed signatures of

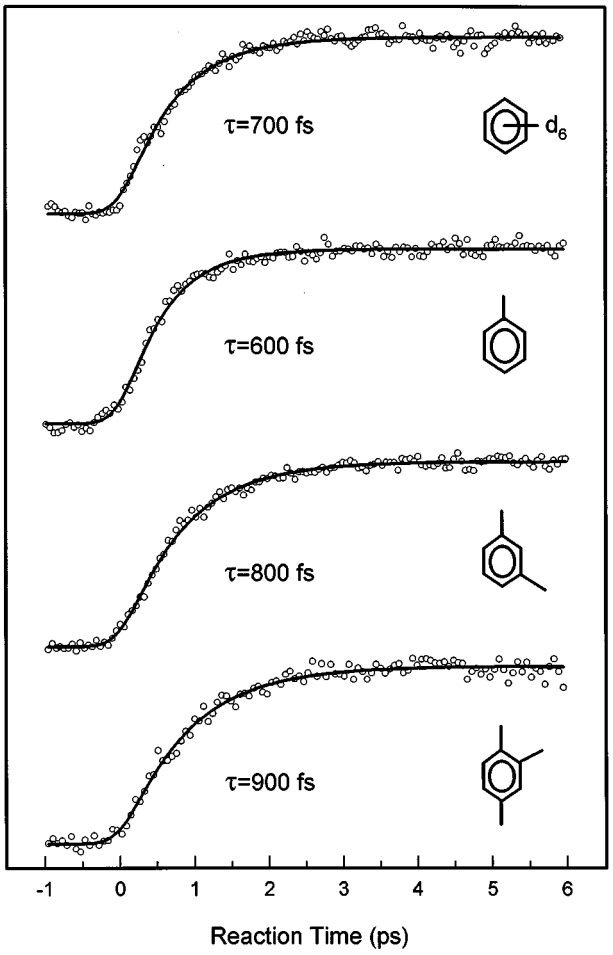

FIG. 11. Typical iodine atom transients resulting from 277 nm excitation of $D\cdot I_2$ complexes. The electron donors for the transients shown here are, from top to bottom, deutrobenzene, toluene, *m*-xylene, and 1,2,4 trimethylbenzene. The apparent rise time constants are indicated for each case.

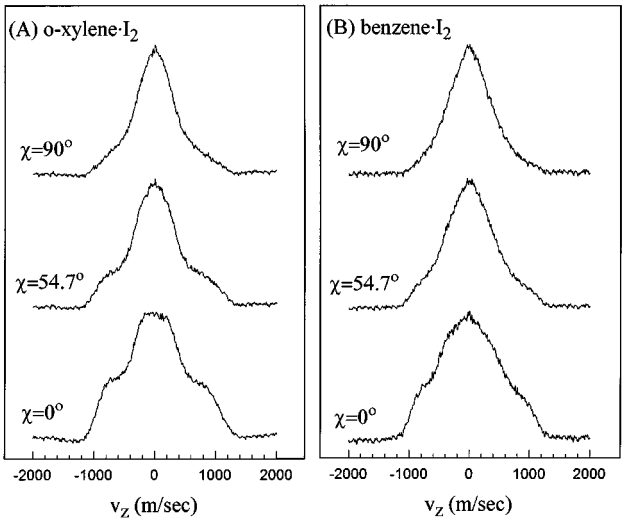

FIG. 12. KETOF (V_z) distributions of iodine atoms resulting from (A) *o*-xylene$\cdot I_2$ and (B) Bz$\cdot I_2$ complexes, excited at 277 nm, for three pump laser–polarization angles (χ) with respect to the TOF-MS axis. The pump–probe delay time was fixed at ~6 ps in both cases.

the underlying reaction mechanisms. Figure 12(A) shows the iodine atom KETOF distributions observed from the *o*-xylene$\cdot I_2$ CT reaction at three pump laser polarizations with respect to the TOF-MS axis. Strictly speaking, they are the v_z distribution since the TOF has been transformed into the v_z domain. These distributions clearly suggest that two distinct components with very different translational energies are present. Using the data analysis procedures described in the Appendix, the two components are unambiguously revealed in the speed distributions derived from the magic angle data, as shown in Fig. 13(A) (upper panel). The higher-speed component peaks at ~1000 m/s and the lower-speed one at ~400 m/s. As discussed in the Appendix, the distribution derived is the speed distribution of iodine atoms with respect to the center of mass (c.m.) of the complex. In order to estimate the relative weights of the two components, the speed distributions were fit to a linear combination of two Gaussian functions (solid line), which were then integrated separately. In this case, the total signal is composed of 45%±5% of low speed component and 55%±5% of high speed component. The choice of the two-Gaussian model is rather arbitrary and is only meant to guide the eyes and to estimate the relative weights.

The speed distribution $g(v)$ is then transformed into the translational energy distribution $P(E_t)$, shown in Fig. 13(A) (lower panel), by the following relations:

$$P(E_t)=\frac{g(v)}{m_I v}, \quad E_t=\frac{1}{2}\, m_I v^2, \tag{5}$$

where m_I is the mass of the iodine atom. Note that E_t is the iodine atom translational energy with respect to the c.m., not the total c.m. translational energy released. We prefer presenting the translational energy in this manner because the exact kinematics associated with the reaction is not clear (two- vs three-body dissociations) and may not be uniform throughout the entire distribution. In the energy domain, the high-energy distribution is centered at ~5000 cm^{-1} and the low-energy one at ~900 cm^{-1}. Note that the *two components do not correspond to two reaction channels separated by the iodine atom spin-orbit energy* (~7600 cm^{-1}). Strong supporting evidence is that, as will be shown below, the two components exhibit markedly different temporal behaviors. Moreover, it will become clear in Sec. V that the iodine atoms resulted from exit channels separated by the spin–orbit energy do not have translational energies consistent with the two components.

The iodine atom transient signal arising from the background I_2 in the molecular beam is not corrected for in the KETOF distributions presented here. However, as shown in the previous section, the total transient iodine atom signal contains only 10%–15% of background signal. Furthermore, the background iodine atom KETOF distribution measured without aromatic donors in the gas mixtures is rather isotropic with no sign of any high-energy wings. Subtraction of

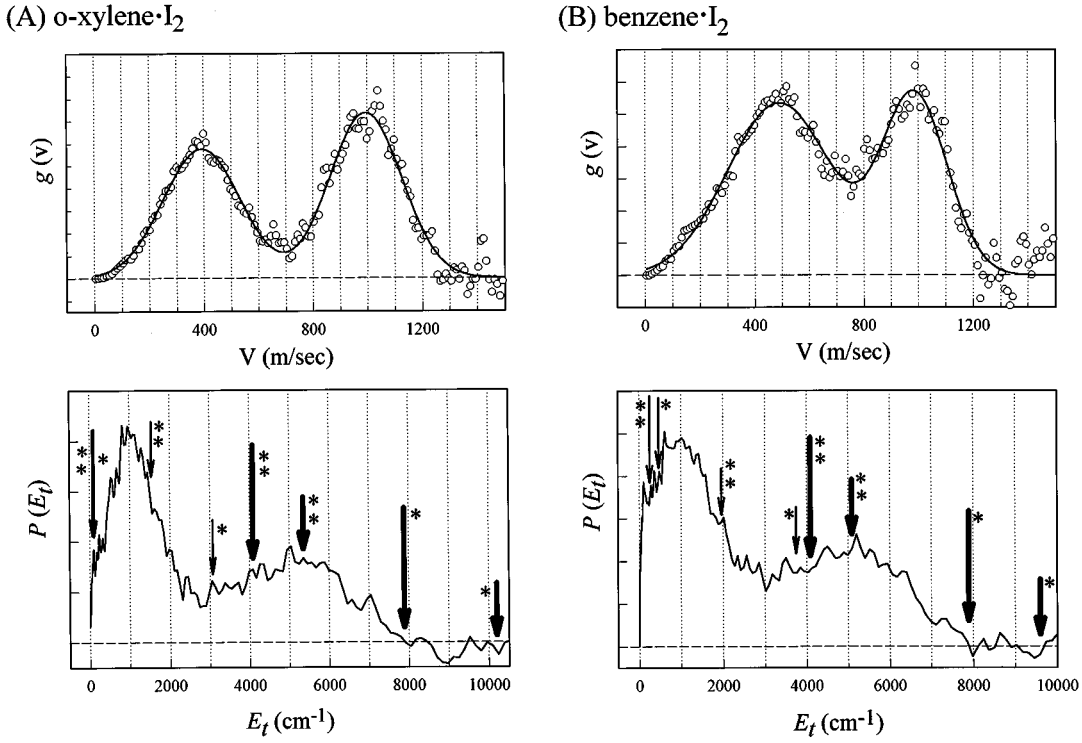

FIG. 13. (A) Upper panel: Recoil speed distribution of free iodine atoms produced from the o-xylene$\cdot I_2$ reaction at a pump-probe delay time of ~6 ps. The open circles are the raw data derived from the magic angle data shown in Fig. 12(A) and the solid line is the result of a two-Gaussian fit. Note that the speed is the relative speed of the iodine atom with respect to the c.m. of the precursor complex. Lower panel: Translational energy distribution of the free iodine atom resulting from the o-xylene$\cdot I_2$ reaction. The long arrows indicate the energies calculated by the first extreme model described in the text, whereas the short arrows are for those predicted by the second extreme model. The thick arrows denote the uncaged iodine atom and the thin arrows denote the caged iodine atom. The accompanied asterisk and double asterisk indicate the dissociation asymptotes I+I* and I*+I*, respectively, along the I–I coordinate in the neutral exit channels. Note that the energy is the relative translational energy of the iodine atom with respect to the c.m. of the precursor complex. (B) Recoil speed and translational energy distributions of the free iodine atoms resulting from the Bz$\cdot I_2$ reaction at a pump–probe delay time of ~6 ps. These are derived from the magic angle data shown in Fig. 12(B). All other aspects are the same as those described in (A).

this background KETOF distribution with a 10% weight from the D$\cdot I_2$ ones eventually results in identical speed distributions as the uncorrected ones.

The KETOF distributions observed for the Bz$\cdot I_2$ reaction, shown in Fig. 12(B), are somewhat different from the o-xylene$\cdot I_2$ ones. The Bz$\cdot I_2$ parallel polarization data also exhibit a high-energy shoulder but is not as obvious as in the o-xylene$\cdot I_2$ case. Nevertheless, as shown in Fig. 13(B), the speed and translational energy distributions obtained from analyzing the magic angle KETOF data again clearly reveal the presence of two distinct components. The high-energy component is similar to the one observed in the o-xylene$\cdot I_2$ case in terms of the peak energy and width. However, the low-energy component is clearly broader and shifted to slightly higher energy, which effectively blurs the appearance of the high-energy component in the KETOF distribution. The low-speed component in the o-xylene$\cdot I_2$ case can be well simulated by a Gaussian function with a center speed of 390 m/s and a width (FWHM) of 330 m/s. However, in the Bz$\cdot I_2$ case, the center speed shifts to 490 m/s and the width becomes 450 m/s. The contribution of the high-energy component in the Bz$\cdot I_2$ reaction was underestimated in our preliminary report[1] partly due to the fact that the low-energy component is broader and higher in energy and partly due to the much longer TOF of I^+ (~23 μs) which discriminates against the higher speed fragments as a result of the longer flight tube and lower acceleration voltages previously used (see Sec. III C).

The recoil anisotropy distribution $\beta(v)$ is then obtained by fitting the parallel polarization KETOF distributions using the speed distribution derived from the magic angle polarization data according to the procedure described in the appendix. Figure 14 shows the $\beta(v)$ of four representative systems along with their iodine atom speed distributions, while Fig. 15 shows two typical results of the fits. Two important features are readily seen in Fig. 14. First, $\beta(v)$'s are definitely positive for all systems at all speeds, indicating a parallel-type transition is dominant. Second, β is close to zero at low speed ($\leqslant$400 m/s). These results are crucial in understanding the CT state dynamics as well as their structures, as discussed below. We shall not focus on the variation of β as a function of speed, instead a weighted, averaged β_{av} is estimated for the low- and high-energy components. The low-energy components have β_{av}'s~0.2–0.3 and the high-energy components have β_{av}'s~0.7–1.0.

Similar KETOF distributions were observed for all other D$\cdot I_2$ complexes that we have studied. The translational energy distributions for these systems are displayed in Fig. 16

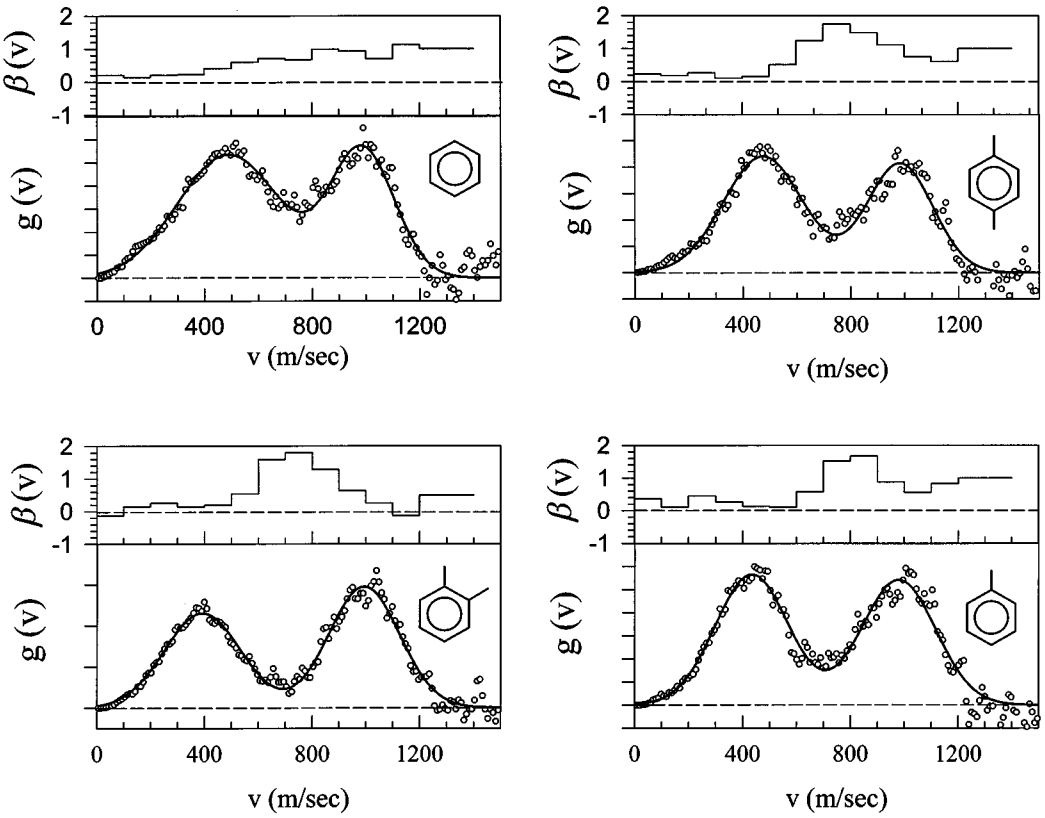

FIG. 14. Recoil anisotropy parameters and speed distributions of the free iodine atoms produced in four $D \cdot I_2$ reactions. The electron donors of the complexes are indicated in each figure and the solid curve in the speed distribution is the result of the two-Gaussian fit.

for comparison. Note that the high-energy components are located at almost exactly the same energy and have similar widths for all systems, whereas the low-energy ones exhibit some dependence on the electron donor. The low-energy components in the $Bz \cdot I_2$ and $C_6D_6 \cdot I_2$ reactions are clearly broader and higher in energy than other systems.

D. Time-resolved KETOF: Dynamics of different channels

We chose the *o*-xylene$\cdot I_2$ reaction as a prototype for the fs time-resolved KETOF studies because it produces clearly separated low- and high-energy components. Figures 17(A) and 17(B) show the temporal evolution of KETOF distributions measured at the magic angle and parallel polarizations, respectively, as the pump–probe delay time increases. The time-resolved translational energy distributions obtained from the magic angle data are displayed in Fig. 18. These data clearly show that there is a strong time dependence in the KETOF distributions. At very early times (0.5 ps) the low-energy component accounts for only about 20% of the total but its weight increases to about 45% at later times (>6 ps), indicating a slower rise than the high-energy component. These results show that the iodine atom transients described in the previous sections are composed of at least two temporal components and that the time constants derived from the single-exponential fit are merely the apparent time scales for the reactions.

To better describe the differences in their time scales, we estimated the contributions of the low- and high-energy components at different times by the procedure described in the last section using the two-Gaussian model. Shown in Fig. 19 are the integrated intensities of the low- and high-energy components plotted against the delay times. The data points of the high-energy component can be simulated by a single exponential rise of 450 fs convoluting with the system response of 500 fs. The low-energy component data, on the other hand, give a single-exponential time constant of 1.4 ps. As discussed in Sec. IV E, we used the CPM laser system to gain better resolution and observe the ~250 fs (mesitylene) component at early times.

E. Transient decay: Initial transition-state evolution

To reveal the motion of the initially prepared CT state of $Bz \cdot I_2$, we have monitored the $Bz \cdot I_2^+$ ion signal as a function of the pump–probe delay time. The idea was to ionize the CT state of $Bz \cdot I_2$ with the 304 nm photons while it is moving through the transition state toward the exit region. However, the transient signal of $Bz \cdot I_2^+$ was extremely weak under the 1:1 complex condition. In fact, even the time-independent signal of $Bz \cdot I_2^+$ was quite weak. This is primarily due to the energetic to ionization as well as unfavorable Franck–Condon factors which cause fragmentation in the parent ions upon two-photon absorption of the CT state at 304 nm.

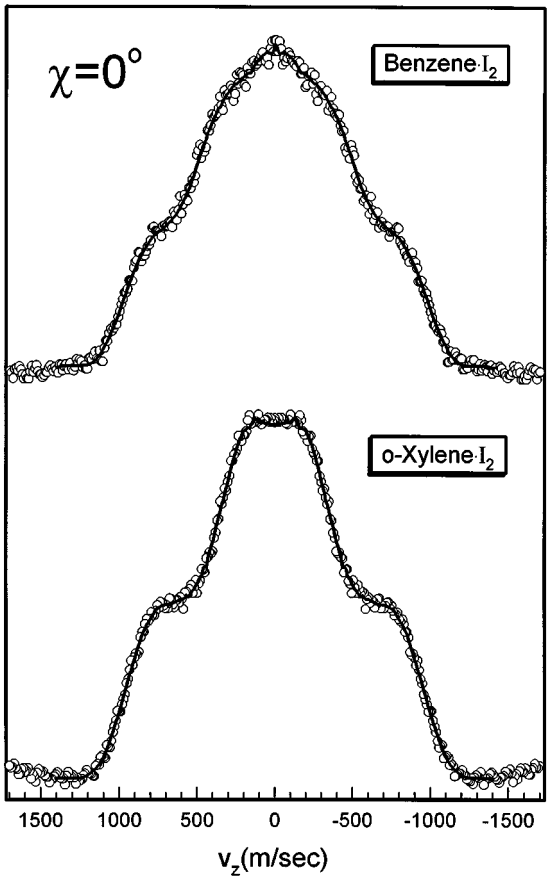

FIG. 15. Typical results of the nonlinear least square fit of the parallel polarization KETOF distributions to the speed distributions derived from the magic angle data using the procedure described in the appendix. The open circles are the raw data and the solid lines are the results of the fit. Since the fitting procedure only uses the first-half ($V_z>0$) of the KETOF distribution, the second-half ($V_z<0$) of the data shown here are the replica of the first-half.

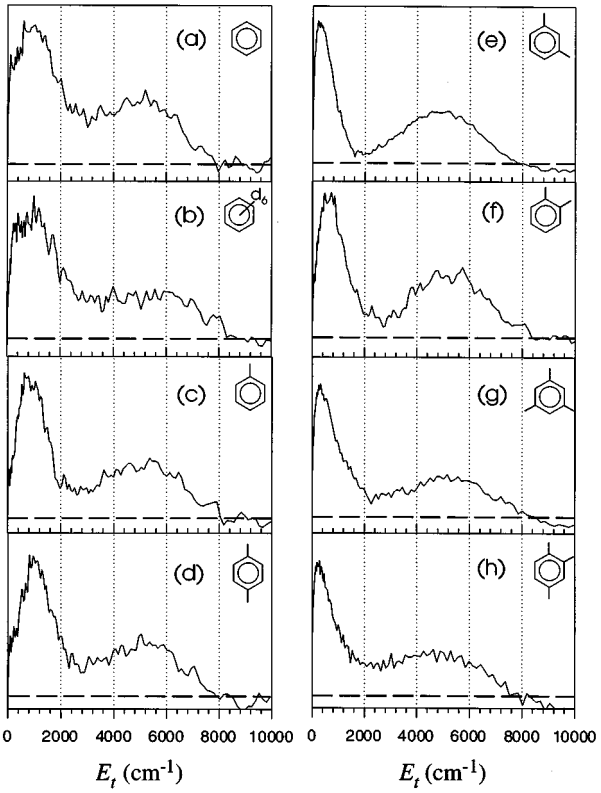

FIG. 16. Translational energy distributions of iodine atoms produced from various $D\cdot I_2$ complexes excited at 277 nm and measured at a pump–probe delay time of ~6 ps. The electron donors of the complexes are (a) benzene; (b) deutrobenzene; (c) toluene; (d) *p*-xylene; (e) *m*-xylene; (f) *o*-xylene; (g) mesitylene; and (h) 1,2,4-trimethylbenzene. Note the broader low-energy components in the cases of $Bz\cdot I_2$ and $C_6D_6\cdot I_2$.

As a result, we observed intense transient signal from the Bz^+ mass channel, as shown in Fig. 20(A) with two different pump–probe polarization orientations. These transients observed in the Bz^+ mass channel resemble the initial dynamics of the $Bz\cdot I_2$ CT state for the following reasons: (1) The transient signal is observed only when Bz and I_2 are simultaneously present in the gas mixture. When benzene vapor was expanded alone with pure He, no transient signal was observed; (2) benzene does not absorb in the pump laser wavelength region (277 nm). Even if it did, the S_1 state of benzene is known to have a lifetime of ~100 ns, whereas the decay we observed here is shorter than 1 ps. The triplet states of benzene are out of the question for the same reason. Hence, these Bz^+ transient signals can only come from the fragmentation of the $Bz\cdot I_2^+$ parent ions, which are produced by the ionization of the $Bz\cdot I_2$ CT state. The observed Bz^+ transient therefore represents the dynamics of the initial CT state. Further support comes from the transient signal observed directly from the $Bz\cdot I_2^+$ mass channel under the larger cluster conditions; the decay is still on a similar time scale. The successful detection of the $Bz\cdot I_2^+$ transient signal under larger cluster conditions is due to the lower IPs and ionic fragmentation of larger $(Bz)_n\cdot I_2$ clusters.

The transients shown in Fig. 20(A) exhibit a biexponential decay behavior dominated by an extremely fast initial decay component. With our cross correlation of ~500 fs, for the synch-pumped laser system, we could only conclude that $\tau_1<200$ fs. The second component is much weaker ($\leqslant 20\%$) and has a decay time constant of ~800 fs. The rapid initial decay of the Bz^+ transients suggests that the $Bz\cdot I_2$ CT state is indeed very short lived (<200 fs). The biexponetial decay behavior of the initial CT state provides some insight into the nature of the TS as discussed in Sec. V.

With the CPM amplified laser pulse (~60 fs) we observed similar decays by monitoring the mesitylene ion signal with $\lambda_{pump}=310$ nm and $\lambda_{probe}=620$ nm. As shown in Fig. 21(B) for the mesitylene$\cdot I_2$ system, the decay is 250 fs, again consistent with the results obtained from time-resolved KETOF and from the detection of Bz^+. The slower decay observed in this case could be a result of the much lower excitation energy (310 vs 277 nm). The long decay component is less than few percent compared to $Bz\cdot I_2$, and this is consistent with the change in the contribution of the two channels discussed next. From these experiments we established $\tau^{\ddagger}$ of the TS to be ~250 fs.

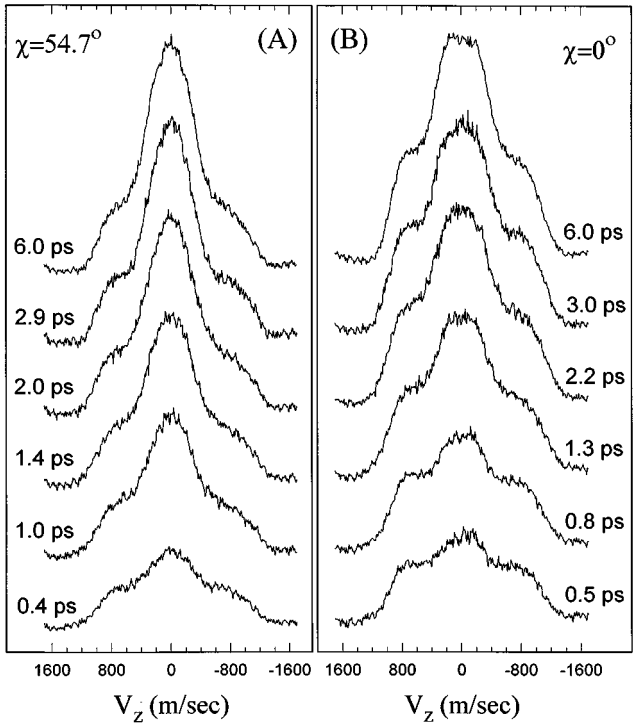

FIG. 17. Time-resolved, KETOF distributions of iodine atoms resulting from the *o*-xylene·I_2 reaction measured at a series of pump–probe delay times. Pump laser polarization is (A) at the magic angle and (B) 0° (parallel) with respect to the TOF-MS axis. The pump–probe delay times are indicated for each distribution.

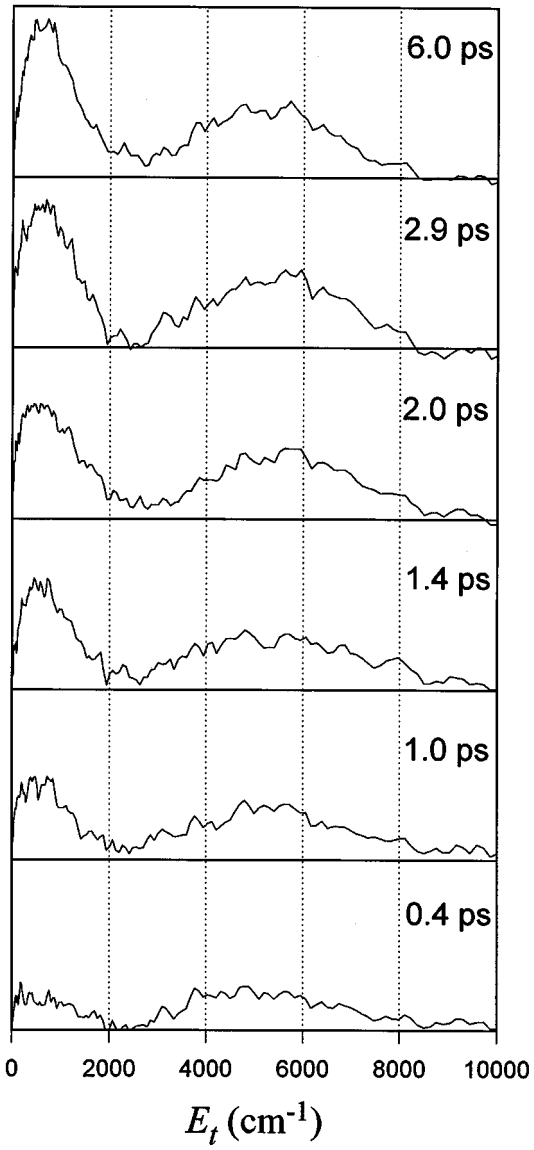

FIG. 18. Time-resolved, translational energy distributions of iodine atoms resulting from the *o*-xylene·I_2 reactions measured at a series of pump–probe delay times. These data are derived from the magic angle KETOF distributions shown in Fig. 17A.

V. DISCUSSION

The experimental results presented above can be briefly summarized as follows: (1) Upon the CT preparation of D·I_2 complexes, iodine atoms are produced very rapidly on a time scale of less than 1 ps; (2) the iodine atom translational energy distributions exhibit two very different components, one which peaks at a low energy (less than 1000 cm^{-1}) and the other at a high energy of about 5000 cm^{-1}; (3) the recoil anisotropy of the iodine atoms is 0.2–0.3 for the low-energy component and is ~0.7–1.0 for the high-energy one; (4) the two components of the translational energy also show different temporal behaviors, the high-energy one rises very rapidly (450 fs), whereas the low-energy component builds up much slower (1.4 ps for D=*o*-xylene); (5) the reaction time decreases with increasing energy and is robust in all MBzs; and (6) following the evolution of the transition states gives a decay time $\tau^{\ddagger}$ of 250 fs. In this section, we will begin by describing the energetics of the system. Then, we will give a description of the dynamics and mechanism, together with elucidation of the initial structure of the TS.

A. The energetics

1. The geometry and TS entrance channel

The nuclear configuration of the initial state is determined by the structure of the Bz·I_2 complex ground state since the reaction is initiated by a vertical excitation. As mentioned earlier, several experimental and theoretical studies have provided evidence that the axial structure is the most stable configuration for Bz·I_2. Recently, our group has also performed *ab initio* calculations at the MP2 (Møller–Plesset perturbation theory) level of theory, and found that the axial structure is more stable than the resting structure by about 2 kcal/mol. The Bz·I_2 molecular structure shown in Fig. 2 is based on these *ab initio* calculations. A detailed account of the *ab initio* results will be published later.[33] For complexes having MBzs as the donors, small deviations from the perfect axial form are expected. In this paper, we will first restrict our discussion to the axial structure for the Bz·I_2 complex and we will show that our experimental results are in fact consistent with the axial rather than the resting structure.

For Bz·I_2, the axial structure belongs to the C_{6v} point

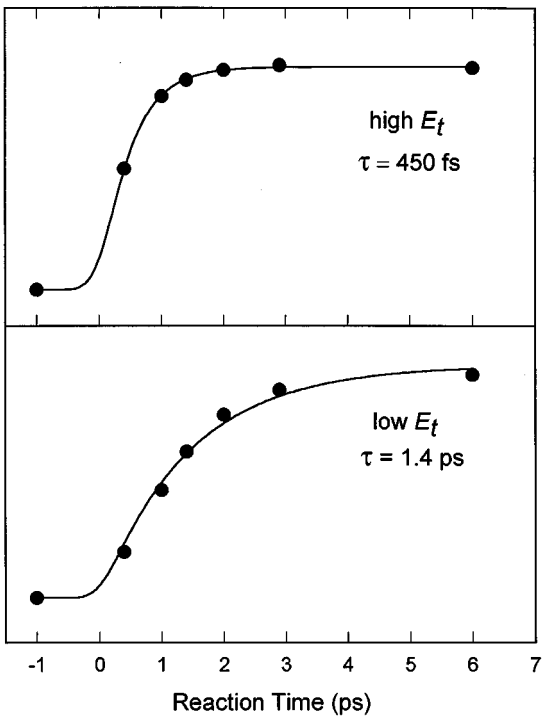

FIG. 19. Plots of the integrated intensities (●) of the low- and high-energy components of the time-resolved, translational energy distributions shown in Fig. 18 against the pump–probe delay times. The solid lines are the results of single-exponential fits to these data points with the system response convolution (see the text).

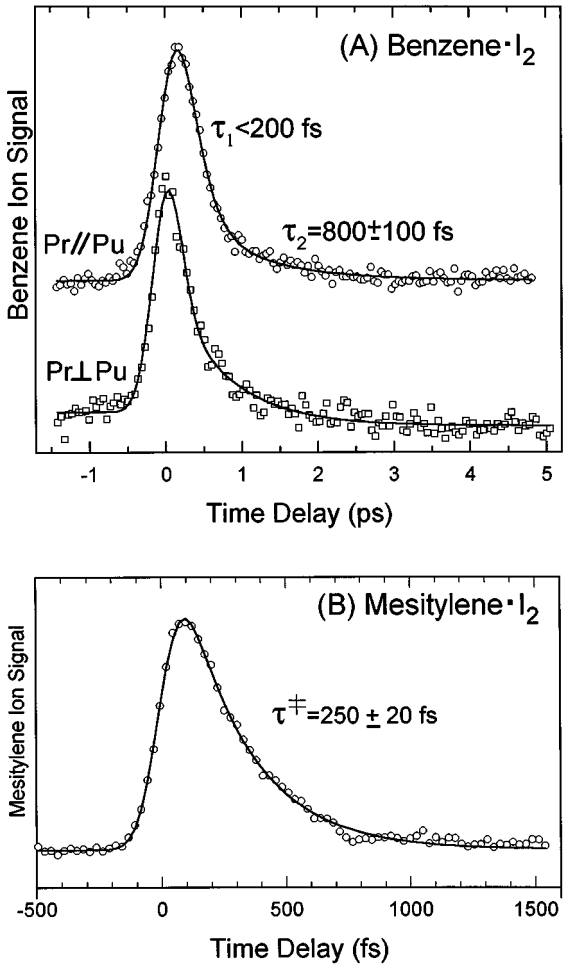

FIG. 20. (A) Transients obtained by monitoring the signal in the Bz^+ mass channel as a function of the pump (277 nm) and probe (304 nm) delay time for the $Bz \cdot I_2$ reaction using the synch-pumped laser system. As described in the text, these transients reflect the dynamics of the initial CT state of $Bz \cdot I_2$. The solid lines are results of biexponential decay fits. (B) Transient obtained in a similar experiment on the mesitylene·I_2 reaction using the CPM laser system. The pump and probe wavelengths are 310 nm and 620 nm, respectively (see the text).

group. In the simplest picture, based on the Mulliken's theory,[10,11] the first CT excitation promotes an electron from the highest occupied molecular orbital (HOMO) (π) of benzene to the lowest occupied molecular orbital (LUMO) (σ^*) of the molecular iodine, as illustrated conceptually in Fig. 21, forming a benzene cation and a molecular iodine anion. The HOMO of benzene is of e_1 symmetry and the LUMO of I_2 is of a_1 symmetry in the C_{6v} complex frame. The electronic symmetry of the first CT state is therefore E_1 in C_{6v}. The degeneracy can be removed by methyl substitutions of benzene and by distortion from the axial structure. The bond energy of I_2^- (1.10 eV) is lower than that of I_2 (1.58 eV) due to an additional electron in the antibonding orbital (σ^*).

At infinite separation between Bz^+ and I_2^-, the asymptotic energy is simply $IP_{ad}(Bz) - EA_{ad}(I_2) = 6.67$ eV, where IP_{ad} and EA_{ad} are the adiabatic ionization potential and electron affinity, respectively. As Bz^+ and I_2^- approach closer, the potential energy is lowered, mainly due to the Coulomb energy $-e^2/R$, until the repulsion between the two moieties becomes significant. In Fig. 22 a schematic potential energy curve (thick solid line) for the $Bz \cdot I_2$ CT state is depicted along the Bz–I coordinate based on this oversimplified picture. The curve is obtained by fitting available spectroscopic information and reasonable estimates for the equilibrium Bz—I_2 separation.

Note that the curve is adiabatic in all internal coordinates of Bz and I_2. Upon CT excitation, internal levels of Bz^+ and I_2^- can also be populated according to their Franck–Condon overlaps with the neutral ground states. To visualize this multidimensional problem, we can think of it as a series of CT potential energy curves which correspond to different internal levels of Bz^+ and I_2^-, along the Bz–I coordinate. One of these curves (the dashed line) which corresponds to the vertical electron attachment of I_2 neutral, is also shown in Fig. 22. The asymptotic energy of this curve is $IP_{ad}(Bz) - EA_{vt}(I_2) = 7.57$ eV, where EA_{vt} is the vertical electron affinity.

The Franck–Condon overlaps in the I_2 and Bz internal and Bz–I_2 intermolecular coordinates govern the initial nuclear configuration reached by the pump pulse. Photoelectron spectroscopic studies[60] have shown that a large fraction of the benzene cation is produced in its vibrationless level upon photoionization of benzene. Although several fundamentals are also excited with small probabilities, these low excitations of the benzene cation modes are rather unimpor-

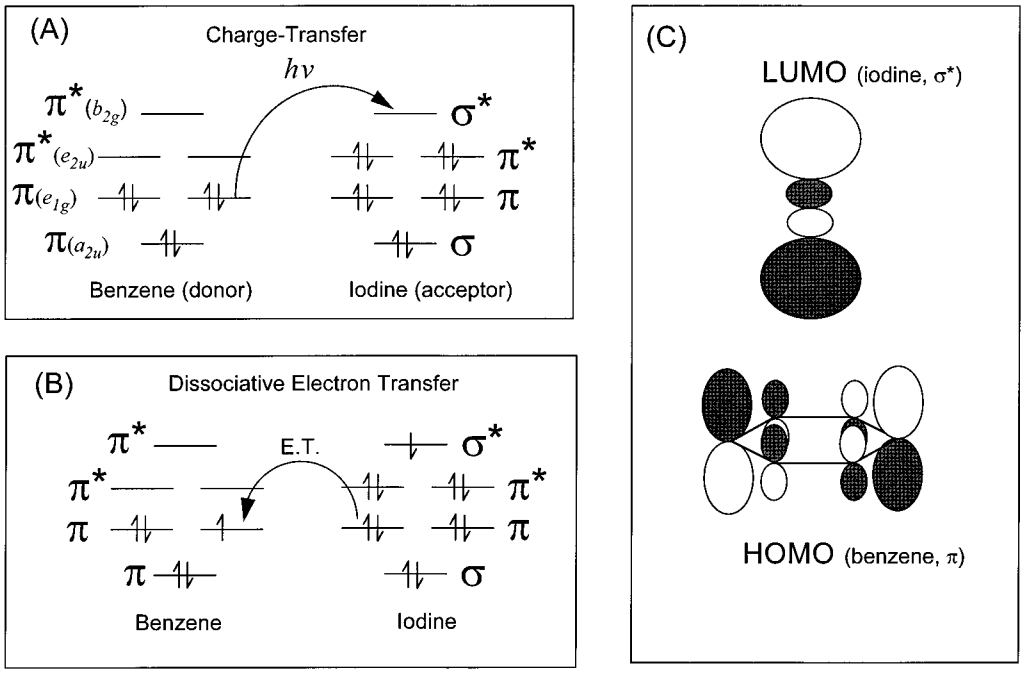

FIG. 21. (A) Schematic diagram showing the electronic configurations of benzene and molecular iodine. The arrow represents the first CT excitation which promotes an electron from the HOMO of the donor to the LUMO of the acceptor. (B) Schematic diagram showing the back electron transfer process which leaves the molecular iodine electronically excited. (C) Pictorial representation of the HOMO (benzene) and LUMO (I_2).

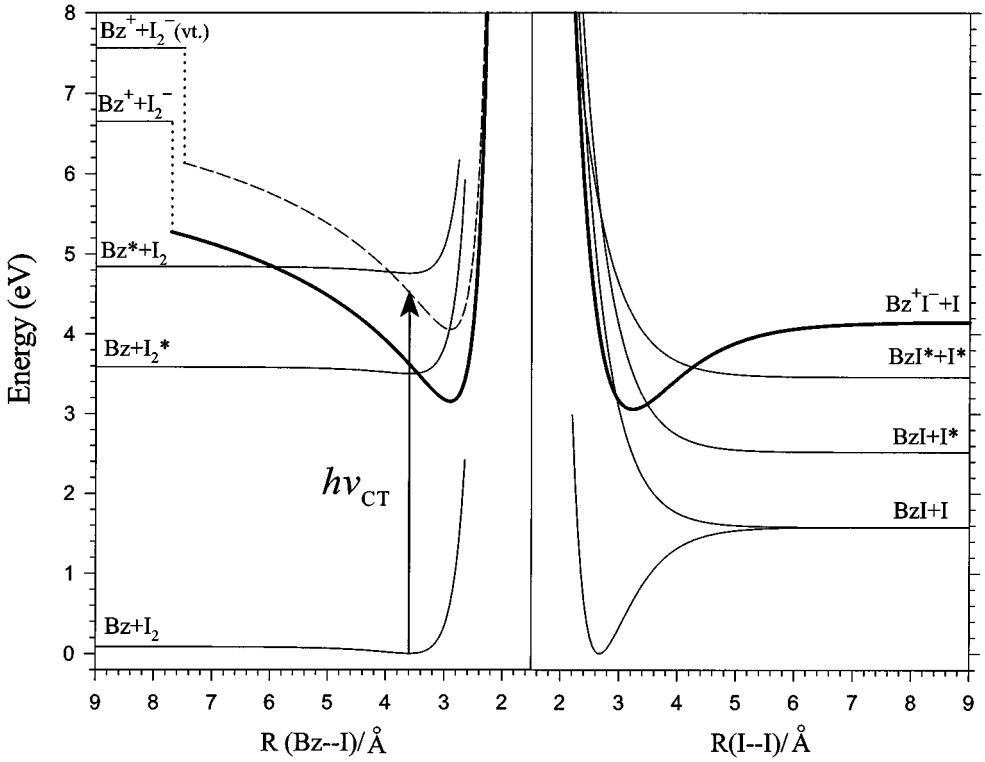

FIG. 22. Potential energy curves along the Bz–I and I–I coordinates. The thick solid curves correlate to the zero-point levels of Bz^+ and I_2^- (also Bz and I_2). The dashed curve shown in the Bz–I coordinate correlates to I_2^- with a vibrational excitation due to vertical electron attachment (see the text for details).

tant in the reactions discussed here, and we shall neglect the benzene cation internal excitation hereafter.

On the other hand, because of the very different equilibrium bond lengths between the neutral and anionic molecular iodine as a result of the additional electron in the antibonding orbital, electron attachment of I_2 is expected to produce I_2^- with a broad distribution of vibrational excitation. Based on the potential energy curves derived by Chen and Wentworth,[61] vertical electron attachment of I_2 should produce I_2^- at some high vibrational levels close to the dissociation limit. In the Bz–I coordinate, the equilibrium separations between Bz and the nearest I atom in the ground (r_e'') and CT states (r_e') of the $Bz\cdot I_2$ complexes are expected to be quite different as a result of the very different intermolecular interactions. Vertical excitation therefore also prepares the initial state with a moderate vibrational excitation in the Bz–I coordinate. The CT absorption bandwidth is simply the result of the broad Franck–Condon envelopes in these two coordinates. The net effect in going toward the blue side of the CT absorption band is to increase the vibrational excitations in both I–I and Bz–I coordinates.

The picture is now clear, at least qualitatively, for the TS entrance channel. At $t=0$, the system is brought to the CT state and the Coulomb potential along the Bz–I coordinate is suddenly turned on—harpooning at these particular separations (see Fig. 1). While the two moieties start executing a large amplitude vibrational motion in the Coulomb potential, I_2 also immediately begins to vibrate upon acceptance of the electron.

A potential energy curve corresponding to a locally excited state which dissociates to $Bz(S_1)$ and neutral I_2 ground state is also shown in Fig. 22. Although the energetics of this state is near our excitation energy, especially for the MBzs, its contribution to the initial state can be ruled out, as mentioned in Sec. IV. However, it is worthwhile to point out that when $Bz(S_1)$ collides with neutral I_2, there is a finite probability that the system can cross and enter the CT state. This is possible because the IP of $Bz(S_1)$ is only 4.48 eV, making it behave like an alkali metal atom capable of ejecting an electron to a flyby I_2 at a large distance and then pull the halogen molecule in to a closer distance by the long-range Coulomb force allowing the reaction to occur. This represents another possible entrance channel that is similar to the harpoon mechanism of alkali/halogen reactions. Note that in our approach the harpooning is directly achieved by fs laser excitation.

2. The product exit channels

We are mainly concerned with the exit channels in the I–I coordinate because the reactions we have probed must involve I–I bond breakage. Schematic potential energy curves of several energetically possible exit channels along the I–I coordinate are depicted in Fig. 22.

a. The ionic exit channel: Harpooning. Once the system enters the CT transition state through the entrance channels, the I_2^- can break apart to give rise to an ionic $Bz^+\cdot I^-$ complex and a neutral iodine atom, provided that it is energetically feasible. Although charge redistributions must take place, the electronic configuration is not changed along this reaction coordinate, i.e., the CT entrance and ionic exit channels are on a single potential energy surface (PES). We will call this PES ''ionic surface'' hereafter. An empirical ionic PES will be presented in section V F.

A potential energy curve is shown in Fig. 22 to qualitatively describe the ionic channel along the I–I coordinate. The curve is simply an I_2^- potential that is offset to match the asymptotic energy of $Bz^+\cdot I^- + I$. This is, of course, a crude approximation since the presence of the benzene cation in the near vicinity must introduce some perturbation to the bonding of I_2^-. The ionic product $Bz^+\cdot I^-$ is simply the CT excited state of the $Bz\cdot I$ complex. The CT absorption band maximum of $Bz\cdot I$ has been reported to be at 430 nm in the gas phase.[39] Based on the available spectroscopic data[39,62] and reasonable estimates for the equilibrium separations, we predicted that the zero-point level of $Bz^+\cdot I^-$ lies at about 2.5 eV above its ground state (see Sec. V F for details). This gives ~0.4 eV of available energy for the $Bz\cdot I_2$ reaction at 277 nm excitation.

For systems with MBzs as the electron donors, gas phase spectroscopic data are not always available. However, liquid-phase studies[63] have shown that there is an excellent correlation between the CT absorption maxima of $D\cdot I$ complexes and the IPs of D. We can therefore estimate the zero-point energy of $MBz^+\cdot I^-$ using $Bz^+\cdot I^-$ as a reference, i.e., $E(MBz^+\cdot I^-)=E(Bz^+\cdot I^-)-\Delta IP$, where $\Delta IP=IP(Bz)-IP(MBz)$.

When the two iodine atoms are separated far enough, the neutral iodine atom product can be readily detected by our probe laser as a free iodine atom using mass spectrometry. The ionic product $D^+\cdot I^-$ complex is very strongly bound (~4 eV). Even though a fraction of the available energy is expected to flow into the $D^+\cdot I^-$ vibration, it is certainly not enough to break it apart. The ionic complex can relax to the ground state either radiatively or nonradiatively and then dissociate. These processes are expected to proceed with much longer time scales and are not observable in our experiments. This expectation is supported by the fact that the lifetimes of CT excited states (B state) of many rare-gas halide complexes, such as XeI, are on the order of 10 ns.[64] Therefore we expect the ionic channel produces only one detectable iodine atom from a $D\cdot I_2$ complex in our experiments.

The ionic exit channel has been observed in many similar systems of bimolecular encounters both in bulk collisions and in weakly bound complexes. For example, in Rg^*+X_2 reactions[65,66] (Rg: rare-gas atoms, X_2: molecular halogens), the Rg atom is first electronically excited by a photon and then the system enters the $Rg^+\cdot I_2^-$ CT state at the ionic–covalent intersection region. The reaction then proceeds through the ionic channel and produces $Rg^+\cdot X^-$ which then decays by slow CT emission. The ionic product CT emission has been widely observed in many cases, including reactions in $Rg\cdot X_2$ vdW complexes.[15] Another example is the famous harpoon reactions $M+X_2$ (M: alkali metal atom).[67] In these reactions, the zero point of the CT state is lower than the neutral reactant asymptote. Therefore, the system can enter

the CT state at the crossing of the ionic-covalent surfaces through thermal bimolecular collisions.

b. The neutral exit channel: Electron transfer. Dissociation of the I–I bond can also take place in the $Bz \cdot I_2$ CT state by coupling to some low-lying I_2 locally excited states that are not bound with respect to the excitation energy. Near our excitation energy, there are many I_2 repulsive states which dissociate into I+I, I+I*, and I*+I*.[56] Three of these states are schematically shown in Fig. 22. Most of these repulsive states are due to ($\sigma \rightarrow \sigma^*$), ($\pi \rightarrow \sigma^*$), and two-electron ($\pi^* \rightarrow \sigma^*$) excitations. The vertical energies of these repulsive states at the equilibrium bond distance of the I_2 ground state (2.66 Å) have been estimated by Mulliken.[56] Some improved vertical energies[68] obtained by calculations including the relativistic effect have been reported recently. The repulsive potential energy curves shown in Fig. 22 were obtained by fitting the curves drawn by Mulliken.[56] It is clear, based on these approximated curves, that the $Bz^+ \cdot I_2^-$ ionic potential must intersect some of these repulsive states in the transition-state region.

If the neutral I_2 locally excited states have the same symmetry as the CT state in the complex molecular frame, surface crossing is avoided and the initial state prepared in the ionic region of the adiabatic surface can exit through regions of neutral characteristics. The branching between the ionic and neutral exit channels depends on the extent of the avoidance (i.e., the ionic–neutral coupling). In the limit of very weak avoidance, the reaction mostly proceeds through the ionic exit channel, whereas in the limit of very strong avoidance the reaction mostly goes through the neutral exit channel.

The result of these mixings is to switch the system, or the transition state, to purely repulsive surfaces that undergo a direct dissociation. A large translational energy disposal is expected from such processes. Hence, the dynamics of the $Bz \cdot I_2$ CT state is expected to be strongly influenced by the nature of the ionic–neutral surface interaction. Although the shape of these repulsive states has not been well determined, the asymptotic energies corresponding to free I or I* are very accurately known. Therefore, the available energies for these neutral exit channels are very certain because the presence of neutral benzene is not expected to alter the I–I bond energy. *Note that when the transition state hops from the ionic surface to the neutral ones, one electron must flow from I_2^- back to the benzene cation. This is equivalent to a spontaneous back electron transfer process*. We will discuss this important point in more detail in Sec. V D.

After the ionic–neutral surface jump, the potential along the I–I coordinate is changed from covalently bound to purely repulsive. On the other hand, the potential along the Bz–I coordinate is switched from a strong Coulomb to a weak van der Waals (vdW) interaction. The fragmentation kinematics is determined by the coupling of the two dissociation coordinates. The nearly direct dissociation of I_2 can release a significant amount of translational energy impulsively. The iodine atom that does not directly face Bz is expected to depart freely without interacting with the rest of the system. However, the one that directly faces Bz may not be able to dissociate promptly without interacting with Bz first. The latter behavior becomes essentially a *one-molecule caging* mechanism similar to the one-atom caging observed in $Rg \cdot HX$[69,70] (X=halogen atom) complexes by other groups. Hereafter, when we discuss the neutral exit channels we will call the iodine atom that directly faces Bz the ''caged iodine atom'', and the other one the ''uncaged iodine atom.'' The binding energy between Bz and an iodine atom is about 0.2 eV at the most.[71,72] Unless the uncaged iodine atom takes away most of the available energy, the caged iodine atom is likely to escape the one-molecule cage, leading to a three-body dissociation.

If Bz and I have a substantial relative velocity when the ionic–neutral switching occurs, Bz–I dissociation can also occur right away because the Coulomb potential that holds the two suddenly disappears. Hence, depending on the crossing points, a fraction of the available energy can be partitioned into the Bz–I coordinate. A neutral vdW potential energy curve is shown in Fig. 22 along the Bz–I coordinate to illustrate this point. The curve correlates to $Bz+I_2^*$, where I_2^* denotes the I_2 repulsive excited states. In this case, the ionic–neutral switching also leads to a three-body dissociation.

B. Dynamics and the mechanisms

Based on the above considerations of the TS entrance and product exit channels, the reaction mechanism can be described by the following elementary steps:

$$[D \cdot I_2]^{\ddagger} \rightarrow [D^+ \cdot I_2^-]^{*\ddagger}$$

$$\rightarrow D^+ \cdot I^- + I \quad \text{(ionic channel)} \tag{6}$$

$$\rightarrow D \cdot I_2^* \rightarrow D+I+I \text{ or } D \cdot I+I, \quad \text{(neutral channels)}, \tag{7}$$

where I_2^* denotes the repulsive excited states of I_2. Note that the I atom products in the neutral channel can either be in the ground or in the spin–orbit excited state.

The available energies for the ionic channels are determined by the zero-point energy of the ionic product $D^+ \cdot I^-$, which in turn, depend on the IPs of the electron donors. As discussed earlier, at 277 nm excitation, the available energy is about 0.4 eV (3200 cm^{-1}) for $Bz \cdot I_2$. Assuming no internal excitation in the products, one finds that the translational energy of the iodine atom is ~2000 cm^{-1} based on the dissociation kinematics. This value is an upper limit, since a large fraction of the available energy is expected to be partitioned into the vibrational excitation of the $Bz^+ \cdot I^-$ product because of the early attractive nature of the PES. The translational energy distribution is therefore expected to peak at a much lower energy and to tail at this threshold energy of ~2000 cm^{-1}. This expectation is consistent with the low-energy components observed in the $Bz \cdot I_2$ and $C_6D_6 \cdot I_2$ translational energy distributions.

For $MBz \cdot I_2$ reactions, the available energies are higher due to the lowering of the IPs in the electron donors. For example, the available energy for mesitylene$\cdot I_2$ at 277 nm excitation is expected to increase to about 1.24 eV (10 000 cm^{-1}). The upper limit for the iodine atom translational energy is ~6600 cm^{-1}, in this case based on the dissociation

kinematics. For systems with toluene and xylenes as electron donors, the upper limits are between those of the $Bz \cdot I_2$ and mesitylene$\cdot I_2$ cases. Therefore, the low energy components observed for the $MBz \cdot I_2$ reactions should tail to higher energies, which is not consistent with the experimental observations. Thus, the contribution of the ionic channel to the low-energy component must be relatively smaller.

As for the high-energy component, the above energetics considerations clearly suggest that it cannot be a direct result of the ionic channel since its energy is too high for all cases. Moreover, as discussed above, the independence of this component on the electron donors is also inconsistent with our expectation for the ionic channel.

In contrast to the ionic channel, the available energies for the neutral exit channels do not depend on the electron donors; they are solely determined by the dissociation limits along the I–I coordinate. At 277 nm excitation, the available energies for the three possible dissociation limits are 1.01 eV (I*+I*), 1.96 eV (I+I*), and 2.9 eV (I+I). In the case of three-body dissociation leading to D+I+I (I*), the available energies would decrease by about 0.1–0.2 eV, which is roughly the binding energy of the D·I ground state. Hence, both the peak energy and the invariance of the high-energy components seem to favor the neutral channels. To support this assignment, we estimate the translational energies of the iodine atoms produced by the neutral channels under two simple, extreme models. In both models, we assume all the available energy goes into the I–I coordinate and consider two extreme kinematics conditions.

In the first extreme model, we assume that no interaction between D and I is encountered during the I–I dissociation, i.e., D is simply a spectator. In this case, all the available energy is partitioned equally into the two iodine atoms' translational energy. For the uncaged iodine atoms, the c.m. translational energies for each iodine atom are 4100 cm^{-1} (I*+I*), 7900 cm^{-1} (I+I*), and 11 700 cm^{-1} (I+I) for the three possible dissociation asymptotes. In Fig.13, these threshold energies are indicated by thick long arrows except for the (I+I) channel which is not within the energy range displayed. Note that this does not imply the (I+I) channel is ruled out because these thresholds are the upper limits. Following the I–I dissociation, the caged iodine atom collides with D with the same amount of translational energy (relative to the c.m. of the $D \cdot I_2$ complex), forming a collision complex well above its binding energy. If we further assume a head-on, elastic collision, we can obtain translational energies of the postcollision iodine atoms, which are 230 cm^{-1} (I*+I*), 450 cm^{-1} (I+I*), and 670 cm^{-1} (I+I) for $Bz \cdot I_2$. These threshold energies are indicated in Fig.13(B) by thin long arrows. For heavier electron donors which are still lighter than the iodine atom, the postcollision iodine atoms have even lower threshold energies, as indicated in Fig. 13(A) for D=*o*-xylene. In fact, based on this simple model, the iodine atom would come to a complete stop if the donor is as heavy as the iodine atom. For example, in the trimethylbenzene$\cdot I_2$ systems where the electron donor is only 7 a.m.u. lighter than an iodine atom, the model predicts the postcollision iodine atom threshold energies to be only 3.3 cm^{-1} (I*+I*), 6.3 cm^{-1} (I+I*), and 9.4 cm^{-1} (I+I).

In the second extreme model, we assume that there is a stiff repulsion between D and I at the moment when I_2 begins to dissociate such that the dissociation first produces an iodine atom and a D·I complex which then subsequently falls apart. For the $Bz \cdot I_2$ reaction, the c.m. translational energies of the uncaged iodine atoms are 5100 cm^{-1} (I*+I*), 9800 cm^{-1} (I+I*), and 14 500 cm^{-1} (I+I). The thresholds are slightly higher for heavier electron donors. For example, for trimethylbenzene$\cdot I_2$, the threshold energies are 5400 cm^{-1} (I*+I*), 10 400 cm^{-1} (I+I*), and 15 400 cm^{-1} (I+I). Note the relatively small variations in going from Bz to trimethylbenzene. These threshold energies are also indicated in Fig. 13 by the thick short arrows. For the caged iodine atom that flies away with D, we assume it somehow separates from D due to the repulsion but does not release significant translational energy. The c.m. translational energy of the iodine atoms thus produced are 1900 cm^{-1} (I*+I*), 3700 cm^{-1} (I+I*), 5500 cm^{-1} (I+I) for $Bz \cdot I_2$. These thresholds are indicated in Fig. 13 by thin short arrows.

These model calculations, of course, oversimplify the dynamics and are only meant to estimate the translational energies to support the proposed mechanism. Note that in the two extreme models, we assume all the available energy is channeled into the I–I dissociation coordinate. This is not strictly valid since a fraction of the available energy may be partitioned into the D–I coordinate, as mentioned earlier. Hence, the threshold energies for the uncaged iodine atoms must be considered as the upper limits for both models. The energies derived for the postcollision iodine atoms in the first model are likely to be the lower limits for the following two reasons. First, the caged iodine atom may acquire more energy if a fraction of energy is channeled into the D–I coordinate. Second, for collisions with finite impact parameters, i.e., not head-on collision, the translational energy loss of the caged iodine atom can be much less. In fact, we will show in a later section that the recoil anisotropy results suggest an oblique structure which is consistent with the latter point.

As can be seen in Fig. 13, all the threshold energies estimated for the uncaged iodine atoms fall in an energy range greater than 4000 cm^{-1} (thick arrows). In particular, the threshold energies for the I*+I* and I+I* dissociation limits are consistent with the high-energy component observed in the translational energy distribution. The broad distribution of the high-energy component is probably due to a distribution of the ionic–neutral crossing points as well as the three possible dissociation asymptotes. On the other hand, the predicted threshold energies for the postcollision iodine atoms fall in an energy range smaller than 4000 cm^{-1} (thin arrows), which is in accordance with the low-energy component. The peak energy of the low-energy component and its dependence on the mass of D agree well with the threshold energies predicted by the first extreme model, i.e., decrease as the mass of D gets closer to that of the iodine atom. Overall, the results of these simple model calculations indicate that both the low- and high-energy components are consistent with the neutral exit channel based on the translational energy considerations.

The observed recoil anisotropy (β) distributions of the iodine atoms also strongly support the neutral, caging mechanism. The averaged anisotropy of the low-energy iodine atoms is clearly lower than that of the high-energy ones for all systems studied. This is consistent with the assignment of the one-molecule caging mechanism, since a large and/or broad distribution of deflection angles is expected for the caged iodine atoms. On the other hand, a higher recoil anisotropy can be expected for the uncaged iodine atom because of its free and nearly direct dissociation. Although the above discussion is based on an axial $D \cdot I_2$ structure, the neutral/caging mechanism is essentially consistent with any structure that effectively intercepts the dissociation of one iodine atom but allows the free departure of the other. On the other hand, if $D \cdot I_2$ assumes the perfectly ''resting'' structure, no obvious interpretation can be made (based on either ionic or neutral exits) regarding the two distinct components in the translational energy distributions and their different temporal behaviors. Hence, our results suggest that the structure of $D \cdot I_2$ is more axial type. Direct evidence of the structure will be discussed in Sec. V C.

The neutral, caging mechanism is also consistent with the time dependence results. The time-resolved KETOF studies show that, at least for the *o*-xylene$\cdot I_2$ reaction, the high-energy component rises within 450 fs. This extremely rapid rise is the characteristic of a direct dissociation, consistent with the high translational energy associated with this component. The time we observed (450 fs) includes the time needed, after electron transfer, for I–I to separate far enough for the free iodine atom detection. Therefore, the electron transfer could actually be much faster than 450 fs. This conclusion is in accordance with the extremely rapid ($<$200 fs) initial state decay observed in the transients shown in Fig. 20, which must be assigned to the time scale for the ionic–neutral surface switching based on this mechanism. The initial state decay exhibits a shorter time scale than the product rise because the wave packet can disperse and move out of the probing region much faster than the formation of the free products.

The low-energy component rises much slower with a time constant of $\sim$1.4 ps. This slowing down is not surprising on the basis of the one-molecule caging mechanism and the 1.4 ps rise simply reflects the lifetime of the collision complex at the given energy. The implication of this time scale to the caging dynamics will be discussed in more details below.

Although only the *o*-xylene$\cdot I_2$ reaction was studied by the time-resolved KETOF, we believe that all other systems are similar in nature. As shown in Fig. 11, the apparent rise of the iodine atoms becomes slower as the number of methyl groups attached on the benzene ring increases, although toluene$\cdot I_2$ is an exception. The apparent rises are simply mixtures of the two components with roughly equal weights. Therefore, if we assume the rates of the ionic–neutral switching are independent of D, then it is the low-energy component that gets slower. Since the available energy for the neutral channel does not depend on the electron donors, the slower rises of the low-energy components indicate that the iodine atom takes a longer time to escape from the one-molecule cage as the number of methyl group increases. This could simply be due to the increase of the D·I binding energy as well as the physical size of D.

Similar arguments can also be applied to the excitation energy dependence of the $Bz \cdot I_2$ reactions shown in Fig. 10, in which the apparent rise times of the iodine atoms are shown to decrease with the excitation energy. Since the available energy for the neutral channel increases with the excitation photon energy, the energy partitioned into the caged iodine atom also increases accordingly. Hence, the excitation energy dependence results suggest that higher energy iodine atoms escape from the one-molecule cage faster.

Overall, the discussions presented in this section suggest that the high-energy component arises solely from the prompt dissociation of the uncaged iodine atoms through the neutral exit channel, whereas the low-energy component is a hybrid of the ionic exit and the neutral, caging mechanisms. The contribution of the ionic channel can be estimated. Since the ionic and neutral channels are parallel exit routes and the ionic–neutral surface jump takes $\sim$200 fs, on the basis of a simple kinetics model, the ionic channel can have a branching percentage of 10% if the time scale for the pure ionic channel is 2 ps, which is a very reasonable estimate based on our trajectory calculations (see Sec. V F). The temporal behavior of the 10% iodine atom products coming from the ionic channel would be difficult to isolate as it should be as fast as the high-energy iodine atoms. The overlap in KETOF distribution makes such isolation difficult to achieve. The low-energy components in the $Bz \cdot I_2$ and $C_6D_6 \cdot I_2$ translational energy distributions have the largest relative weights ($\sim$60%) and are also the broadest among all systems studied. A plausible interpretation is that, in $Bz \cdot I_2$ and $C_6D_6 \cdot I_2$ reactions, the ionic–neutral surface switching is relatively slower so that the branching ratio for the ionic channels is higher. This could be due to the symmetry constraint imposed by the highly symmetric benzene (and also C_6D_6) moiety which makes the ionic–neutral coupling weaker. These symmetry constraints are probably more relaxed in MBzs, and the very efficient ionic–neutral surface coupling in $MBz \cdot I_2$ captures the trajectories toward the covalent exit.

More direct evidence of the existence of the ionic channel is the biexponential behavior observed in the initial state decay of $Bz \cdot I_2$ shown in Fig. 20. The small component ($<$20%) of $\sim$800 fs can be assigned to an intermediate state leading to the ionic channel. Further discussion of this point will be made in more detail in Sec. V D.

C. The structure

An important result obtained in this work is the recoil anisotropy parameter β of the iodine atom products. The values of β are obtained experimentally for both channels of the reaction and are all larger than zero, not negative. The lower averaged β's of 0.2–0.3 for the low-energy component reflect cage exit dynamics which takes $\sim$1 ps. For all systems studied, the averaged β's of the high-energy components are $\sim$0.7–1.0. From the time-resolved experiments, we

know that the high-energy iodine atoms are produced in less than 450 fs. In such a prompt dissociation, the effects of rotational and vibrational motions are negligible, especially under our cold beam condition. The averaged β's therefore suggest that the recoil direction is tilted away from the transition dipole moment by an angle of $\sim 35°$–$40°$. In order to fully understand the correlation between the recoil velocity $\mathbf{v}$ and the transition dipole moment μ we consider the direction of μ in relation to the structure.

First, we briefly review Mulliken's resonance-structure theory for the CT transition in an electron donor–acceptor (D–A) complex.[10,11] The main idea of Mulliken's theory is that the complex is an admixture of the ''no-bond'' and the ''dative bond'' structures. The ground-state wave function of the D–A complex can be written as

$$\Psi_N = a\phi_0(\mathrm{D–A}) + b\phi_1(\mathrm{D^+ – A^-}), \tag{8}$$

where ϕ_0(D–A) is the no-bond configuration wave function and $\phi_1(\mathrm{D^+–A^-})$ is the dative CT configuration wave function. An important requirement for the mixing is that ϕ_0 and ϕ_1 need to be of the same symmetry in the entire D–A complex frame. The first CT state wave function is primarily dative and has the form

$$\Psi_E = a^*\phi_1(\mathrm{D^+–A^-}) - b^*\phi_0(\mathrm{D–A}). \tag{9}$$

Note that in the generalized version of this theory,[11] higher energy CT as well as the locally excited configurations have been included.

The electric dipole transition moment corresponding to the CT excitation can be given by

$$\mu_{\mathrm{CT}} = \langle \Psi_E | \hat{\mu} | \Psi_N \rangle = a^* b \mu_{11} - ab^* \mu_{00} + (aa^* - bb^*)\mu_{01}. \tag{10}$$

μ_{00} and μ_{11} are simply the static dipole moments of the neutral no-bond and ionic dative configurations, and μ_{10} is the transition dipole moment between them. If D and A are both centrosymmetric, such as Bz and I_2, then $\mu_{11} \propto e\mathbf{R}$, where $\mathbf{R}$ is the vector pointing from the ''center of charge'' of D^+ to that of A^-. Hence, for typical vdW separations the magnitude of μ_{11} is on the order of 20 D. On the other hand, μ_{00} should be nearly zero or much smaller than μ_{11}, and Eq. (10) reduces to

$$\mu_{\mathrm{CT}} \approx a^* b \mu_{11} + aa^* \mu_{10}. \tag{11}$$

Therefore, the CT transition is dominated by the two major components. μ_{10} has been shown by Mulliken[10,11] to be roughly proportional to the spatial overlap of the donating and accepting orbitals. Since D and A are in a vdW contact, this component is expected to be small, although Mulliken[11] later pointed out that this term may be important due to the larger size of the accepting orbital. On the other hand, μ_{11} can be very large as mentioned above. The orientation of μ_{11} is rather invariant in the complex, pointing roughly from the center of mass of D to that of A. However, the contribution of this component is largely reduced because the mixing coefficient b is usually small. In particular, if the mixing is forbidden by symmetry, then the first term in Eq. (11) vanishes.

It is difficult to judge the relative importance of the two components based on the above discussion and it might differ from case to case. However, the μ_{10} component alone is certainly not enough to explain the observed strong CT transition in D/I_2 systems. The μ_{11} term should dominate the CT transition whenever the ionic–neutral mixing is enhanced. The manifestation of this effect can be found in the strongly enhanced $D\cdot I_2$ CT absorption intensity in solutions where the mixing can largely be enhanced by lowering of the symmetry as well as by solvation.

Having discussed the CT transition dipole moment, we now use $Bz\cdot I_2$ as a prototype and explore three possible structures considered by Mulliken,[10] namely the ''axial,'' ''resting,'' and ''oblique'' structures, as schematically shown in Fig. 23. In the cases of the resting and oblique structures, the azimuth angle is arranged such that a plane of symmetry (xz) perpendicular to the benzene molecular plane is retained. It should be noted that the resonance theory considered here was developed to account for the very large oscillator strength and spectral shifts as a result of CT. Vibronic coupling and Jahn–Teller effects of the neutral species will not alone describe such changes. However, such effects can be included in the CT description and will illustrate the effect of the nuclear distribution on μ's.

In the case of the *axial structure*, the complex belongs to the C_{6v} point group. The ground state is of A_1 symmetry, and the CT state is of E_1 symmetry. Based on group theory, the CT transition dipole is polarized in the benzene molecular plane. Since the CT state and the ground neutral state are of different symmetry, mixing between them is not allowed. Thus, no transition dipole component perpendicular to the benzene plane is present in the perfectly axial structure. *In this case, the transition dipole is perpendicular to the recoil direction of the high-energy iodine atom and the limiting value for β is -1. Obviously, this is in direct contradiction to the experimental results of β being positive.*

If the complex assumes the *resting structure*, the point group of the complex is C_{2v}. The ground state is still A_1, but the CT state is split into two states with A_1 and A_2 symmetries due to the removal of the degeneracy. The transition from the ground state to the A_1 CT state is allowed and is perpendicular to the benzene plane. In this case, the CT transition can arise from both μ_{11} and μ_{10} terms as the A_1 ionic configuration can mix with the A_1 neutral configuration. The transition to the A_2 CT is forbidden. *Therefore, the transition dipole is also perpendicular to the recoil direction and the limiting value for β is -1, which is again in contradiction to the experimental findings*. Furthermore, the resting structure is not consistent with the observed two translational energy components from which a caging mechanism must be included.

In the case of *oblique structure*, the complex has a C_s symmetry. The ground state is of the A' symmetry and the CT state is again split into two states with A' and A'' symmetries. Transitions from the ground state to both CT states are allowed. The transition to the A'' state is polarized in the benzene plane and perpendicular to the symmetry plane. This transition cannot be the dominant one since the transition

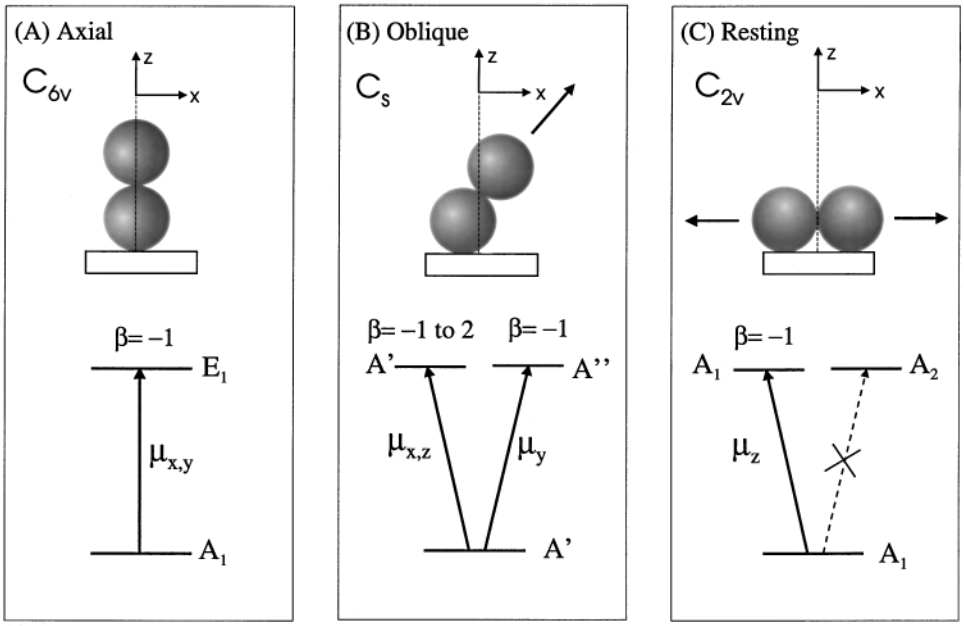

FIG. 23. Pictorial illustration of the three structures considered for the $Bz\cdot I_2$ complex: (A) axial, (B) oblique, and (C) resting. The two balls represent the iodine atoms and the rectangle the benzene plane. In (B) and (C), a plane of symmetry (xz) is retained. The ground and CT state symmetries and the associated transition dipole orientations are also shown for each case, as described in the text.

dipole is perpendicular to the recoil direction and thus $\beta=-1$. For the transition to the A' state, by group theory the transition dipole is polarized in the plane of symmetry. However, Mulliken's theory shows that this transition can have a component perpendicular to the benzene plane. This is because the A' ionic configuration can mix with the A' neutral configuration to give rise to a nonzero μ_{11} term. On the other hand, the orientation of μ_{10} corresponding to the transition from the pure no-bond ground state (A') to the pure dative-bond ionic states (A') is only known to be polarized in the plane of symmetry. However, its exact orientation should follow a smooth evolution when the complex is transformed from axial to resting structures. Hence, for small tilting angles, the complex is more like an axial structure and μ_{10} should be more parallel to the benzene plane. Likewise, for large tilting angles, μ_{10} should be more parallel to the norm of the benzene plane. Combining both μ_{11} and μ_{10}, it is possible to obtain an I_2 tilting angle θ such that the angle between the CT transition dipole and the recoil direction is about 35° which gives a theoretical β value of $\sim+1.0$, consistent with the experimental results.

Based on the above considerations, our results suggest that the $Bz\cdot I_2$ structure is neither axial nor resting, since we clearly observed positive values for β's. The only possible structure that can account for the observed β is the oblique structure. This conclusion does not conflict with the many experimental and theoretical predictions that the axial structure is the most stable form. For a stable axial structure of $Bz\cdot I_2$, our results simply suggest that I_2 is undergoing a large amplitude torsional motion at the moment when the complex is excited. This is to be expected even for the zero-point level because of the relative flatness of the potential energy along the I_2 internal rotational coordinate. Thus, when the $Bz\cdot I_2$ CT state is prepared by fs laser pulses, the wave packet is launched at a nuclear configuration resembling an oblique structure, as schematically shown in Fig. 24. This picture brings to focus the importance of the angular part of the potential between Bz and I_2, similar to the case of $Rg\cdot HX$.[73]

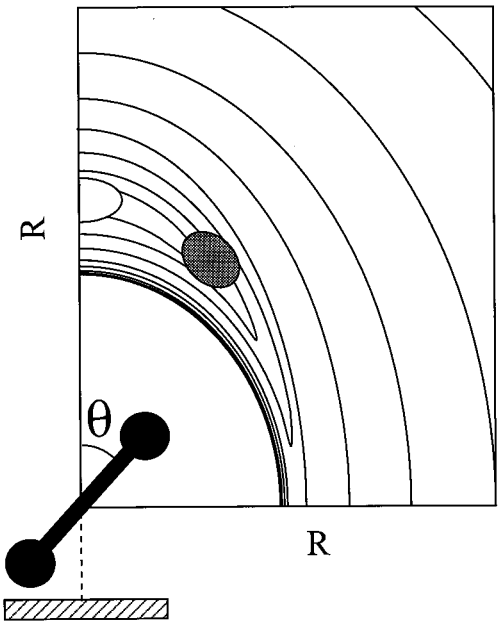

FIG. 24. PES contour map of the $Bz\cdot I_2$ complex in a polar representation $V(R,\theta)$, where R is the distance between the c.m.'s of the two moieties and θ is the I_2 pivoting angle around its c.m. The shaded rectangle represents the benzene molecular plane. The PES has a global minimum at $\theta=0$ (white spot). However, the wave packet in the initial CT state can be prepared at some finite angle (gray spot) because of the large amplitude torsional motion and the much enhanced transition dipole moment at large θ.

Furthermore, in this quasiaxial structure of lower symmetry, the wave packet sample transitions are greatly enhanced by the μ_{11} component, which might therefore dominate the CT excitation. At the exact axial geometry μ_{11} is zero and the system utilizes the much weaker μ_{01} contribution.

This conclusion is in good agreement with the results of recent semiempirical calculations concerning the transition dipole of $Bz\cdot I_2$ reported by the Wiersma group.[42] The main conclusion of their calculations is that the transition dipole component parallel to the benzene plane is always much smaller than the perpendicular component. With the exception of the perfectly axial conformation, the direction of the transition dipole moment was found to be pointing (within $\sim 10°$) from the center of the benzene ring to the I_2 c.m. for all investigated structures including the three forms we have considered above. For the perfectly axial structure, they found that although the transition dipole is polarized in the benzene, its oscillator strength is ~ 200 times smaller than the maximum value found at a tilting angle of $\sim 30°$. Thus, their calculations suggest that the μ_{11} component is much more important than the μ_{10} component, making the transition dipole always perpendicular to the benzene plane. Since the experimental studies by Lenderink *et al.*[42] were conducted in solutions, the excitation of tilted configurations is done by photoselections through the $\mu\cdot\epsilon$ interaction.

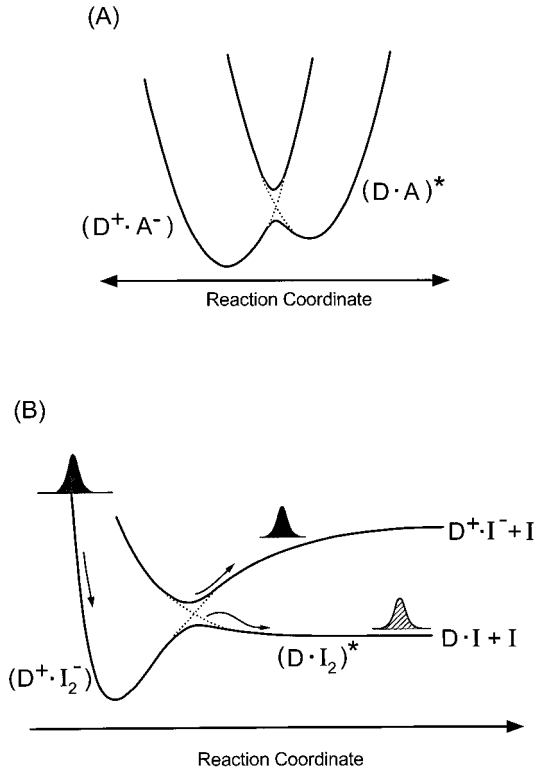

FIG. 25. (A) Potential energy curves along the reaction coordinate for generic charge–transfer reactions. (B) Potential energy curves along the reaction coordinate for dissociative charge–transfer reactions of $D\cdot I_2$ discussed in this paper.

D. The electron transfer: Ionic/neutral branching

The ionic–neutral surface switching is eventually an intermolecular back electron-transfer process as a result of the mixing between the CT and neutral locally excited I_2 repulsive states. This process of ionic–covalent coupling is widely present in many chemical and biological D–A systems[74] where both ionic and covalent states are bound, as generically shown in Fig. 25(A). A schematic representation of the potential energy curves along the reaction coordinate for the present system is also shown for comparison in Fig. 25(B). The final state in the present system is repulsive and leads to an irreversible dissociative electron transfer. The observed initial CT state decay (~ 250 fs) and the high-energy iodine buildup (~ 450 fs) thus provide the important time scales for the intermoelcular electron transfer between D^+ and I_2^-. Upon CT excitation, an electron is promoted from the HOMO (π) of benzene to the LUMO (σ^*) of I_2, creating an ''electron–hole'' pair in the complex (see Fig. 21). One of the electrons in the inner orbitals (σ, π, and π^*) of I_2 then rapidly jumps back to benzene in ~ 250 fs, producing an excited state of I_2 at the same energy as the initial CT state. On the other hand, the return of the σ^* electron originally promoted is greatly hindered by the large energy gap and may have to be accompanied by a radiative decay which is a much slower process.

In the limit of crossing or very weak avoidance, the reaction will dominantly proceed on the ionic potential. We have shown that this is not the case for the present systems since we clearly identify a large fraction of the iodine atom product arising from the neutral exit channel. In the limit of very strong avoidance, the reaction will mostly proceed through the lower adiabatic surfaces shown in Fig. 25(B), but the system switches its character from being ionic to being covalent at the avoidance region. This picture is consistent with our conclusion that the neutral channel is an important exit route, suggesting that a strong surface avoidance exists along the seam near the region where the two surfaces intersect. Depending on the exact shape of the two surfaces, a barrier to dissociation may exist as a result of the avoided crossing and can influence the dissociation. The probability for crossing can be calculated using the Landau–Zener formalism, as applied for the harpoon reaction of NaI.[75]

Based on Mulliken's predictions,[56] there are at least 15 neutral repulsive states that can intersect the ionic surface of $Bz\cdot I_2$, including singlet and triplet states. Not all of these states have the right symmetry to mix with the ionic state. In the perfectly axial structure, the electronic symmetry of the $Bz\cdot I_2$ CT state is E_1. However, there are only 3 out of the 15 states that are of the π symmetry which transforms into E_1 under C_{6v} point group. On the other hand, if $Bz\cdot I_2$ assumes an oblique structure, the symmetry constraint is greatly reduced. The electronic symmetry of the split CT states are A' and A''. Since transition from the ground state to both CT states is allowed, all 15 I_2 repulsive states are allowed to mix with the ionic states by symmetry. Since all neutral and ionic channels are parallel exit routes of the initial state, the ionic channel is suppressed simply by the outnumbered neutral

exit channels. The symmetry constraint can also be relaxed in $MBz\cdot I_2$ reactions even for the axial structure. Therefore, the extremely fast and similar time scales observed for the back electron transfer process in the $Bz\cdot I_2$ and $MBz\cdot I_2$ reactions give further support to the conclusion that the initial CT state is oblique. In solutions, as discussed in Sec. V G, the effective coupling is enhanced due to the instantaneous symmetry breakage by the solvent molecules.

There is no doubt that if all neutral channels could be turned off, the ionic channel can proceed as expected. In cases where the avoidance of the two surfaces is not so strong, the wave packet encountering the avoided region can have a small but finite probability to transmit across to the upper adiabatic surface. The wave packet entering the upper surface can either decay back to the lower surface through the same small transmission probability or proceed through the ionic part of the surface if energetically possible. Thus, depending on the rates of the two decay paths, the wave packet can be trapped in the upper surface for a long period of time. This gives the system a finite probability to proceed through the ionic channel and the transient buildup of its products will exhibit a different temporal behavior from the neutral channel.

Two pieces of evidence support the above points. First, the initial CT state decay for $Bz\cdot I_2$ exhibits a biexponential behavior, as shown in Fig. 20(A). The smaller component of $\sim$800 fs can be assigned to the decay of the wave packet that is trapped in the upper adiabatic surface and the rate (1/0.8 ps^{-1}) is the sum of both the ionic channel and the crossing back to the lower surface. For the mesitylene$\cdot I_2$ system, Fig. 20(B), the smaller component is not as prominent. This is consistent with the smaller ionic branching ratio due to the lowered symmetry. Second, in $Bz\cdot I_2$ and $C_6D_6\cdot I_2$ reactions, the low-energy components observed in the iodine atom translational energy distributions weigh more than those in other reactions. This could be a result of larger ionic branching ratio in these two reactions due to the reduced ionic–covalent mixing caused by the highly symmetric donors involved.

E. One-molecule caging

To describe the encounter of the caged iodine atom with the donor molecule, one has to consider the binding energy of the D·I complex and the relative collision energy between D and I. The D·I complexes have been shown in general to be more strongly bound than their corresponding molecular iodine complexes.[71] In particular, the heat of complex formation of *o*-xylene–I in solution has been reported to be -4.4 kcal/mol,[72] whereas that of the $Bz\cdot I_2$ complex is only about -2 kcal/mol. Therefore, the binding energy of the *o*-xylene–I complex could be as high as 1500 cm^{-1}. In the first extreme model discussed in Sect. V B, the relative collision energies in the c.m. frame of D and I are $\sim$1800 cm^{-1} (I*+I*), 3600 cm^{-1} (I+I*), and 5400 cm^{-1} (I+I) for the three dissociation asymptotes. In the limit of the second extreme model, the collision energy is assumed to be zero and the available energy is partitioned between the uncaged iodine atom and the newly formed D·I complex. Therefore, the relative collision energy is expected to be lower than the values predicted by the first extreme model if the actual kinematics is somewhere between the two extreme cases. On the other hand, if a fraction of the available energy is initially in the D–I coordinate upon I_2 dissociation, the D–I collision energy can be higher. Overall, it is plausible that the observed 1.4 ps rise time is a result of the low collision energy and strong D–I binding. We will show in Sec. V F that this feature of relatively long dissociation times can be reproduced in molecular dynamics (MD) simulations. In addition, if the $D\cdot I_2$ complex has an oblique structure, a finite impact parameter exists for the D–I collision and the associated centrifugal barrier may play a role in slowing down the dissociation.

Another consideration is that, during the collision, some available energy is channeled into the internal modes of D's, reducing the energy available for dissociation, and lengthening the complex lifetime. This $T-V$ process is expected to be rather inefficient within the observed dissociation time scales owing to the weak coupling between the D internal modes and the D–I intermolecular vdW mode. The ''inverse process'' of $V-T$ by predissociation typically takes 10–100 ps.[76] However, if the D–I collision results in a collision complex of new chemical identity as an intermediate toward chemical reactions, the energy can be transferred to the internal modes of D in a short period of time through a much stronger chemical interaction. The 1.4 ps is then the lifetime of this ''chemical'' collision complex. This channel is supported by the results of a cross-beam experiment on a similar system of ''Br+chlorotoluene'' reactions,[77] for which the collision complex was found to have a lifetime not much shorter than a rotational period ($\sim$5 ps) at collision energies of 20–35 kcal/mol. The translational energy disposal was also found to be very low, indicating that a significant amount of the available energy ends up in the internal vibrational modes of the aromatic ring. Although the collision energies in our case are below the threshold for the ring substitution ($\Delta H^\circ + 1.84$ eV for Bz) and hydrogen atom abstraction ($\Delta H^\circ \sim +1.65$ eV for ring H) reactions, they may be above the barrier to some ''transition state'' such as ''iodocyclohexadienyl,'' which can have a finite lifetime long enough for the available energy to be distributed into the internal modes of the ring through a much stronger interaction. In this regard, the caging is fulfilled by chemical forces instead of the physical vdW interactions. What is clear is that the observed dynamics of the complex indicate its 1 ps duration. The complex can engage the vibrational phase space during the ps duration and breaks up by exit channels on a potential determined by the physical/chemical forces (see MD in Sec. V F).

F. Molecular dynamics

Classical trajectory calculations were performed on empirical PESs for both the ionic and neutral exit channels. The purpose of these calculations was to provide a qualitative picture of the reaction dynamics. To simplify the task, we

treated, given the time scale involved, the donor as a point mass with no internal degree of freedom. No angular part is included in the PES and the D–I–I system is assumed to be collinear. In the following discussion, r_1 is the I–I separation and r_2 is the D–I separation. Empirical PESs are constructed by summing the potentials along r_1 and r_2 coordinates, i.e., $V(r_1,r_2)=V_1(r_1)+V_2(r_2)$.

Trajectories were obtained by solving the equation of motion through numerical integration with a fixed time interval of 0.5 fs. The calculations were checked by making sure that the c.m. of the system was immobile and the total energy was conserved over the period of the calculated trajectories with satisfactory accuracy. The production of a free iodine atom is detected whenever the criterion of r_1 and/or $r_2 \geqslant 8$ Å is reached. The final speeds of the free iodine atoms were calculated with respect to the c.m. of the D–I–I system. We could also simulate the decay of the initial transition state by following the trajectory from $t=0$ and the motion in the transition state region. Only representative trajectories were calculated by launching the initial configurations at estimated r_1 and r_2. No attempt was made to average a large number of trajectories as the purpose of the current calculation is only to provide guidance and support to the proposed microscopic elementary steps.

1. The ionic channel: Harpooning

The PES for the CT state is constructed by combining a $Bz^+\cdot I^-$ Coulomb potential and an I_2^- Morse potential. The $Bz^+\cdot I^-$ potential has the following form:

$$V_2(r_2)=\frac{C_{12}}{r_2^{12}}-\frac{C_1}{r_2}. \tag{12}$$

The two parameters ($C_{12}=1.159\times10^5$ eV Å^{12} and $C_1=11.4$ eV Å) are obtained by simultaneously fitting $Bz\cdot I_2$ and $Bz\cdot I$ absorption maxima, 268 and 430 nm, respectively, and by estimating the $Bz^+\cdot I^-$ equilibrium separation of 2.9 Å. The ground state Bz–I equilibrium separation is assumed to be 3.6 Å in the fit. The parameter C_1 is smaller than the theoretical value of 14.42 eV Å, reflecting either an incomplete charge-transfer or localized charge distributions. The I_2^- Morse potential is the one given by Chen and Wentworth:[61]

$$V_1(r_1)=-2k_AD\ \exp[-k_B\beta(r_1-r_e)] + k_RD\ \exp[-2k_B\beta(r_1-r_e)]. \tag{13}$$

The parameters are given in Ref. 61.

For the $Bz\cdot I_2$ reaction, our 277 nm excitation is near the $Bz\cdot I_2$ CT absorption maximum and the initial CT configuration should be near the ground state equilibrium separations in both I–I and Bz–I coordinates. We calculated several trajectories with initial configurations within the range of ($r_1=2.62$–2.66 Å, $r_2=3.6$ Å), which correspond to available energies of ~0.3–0.5 eV. The reaction times for these trajectories are in the range of 1.0–2.4 ps, and the final speed of the neutral iodine atom is in the range of 100–650 m/s. Figure 26(A) shows a typical trajectory on the ionic PES.

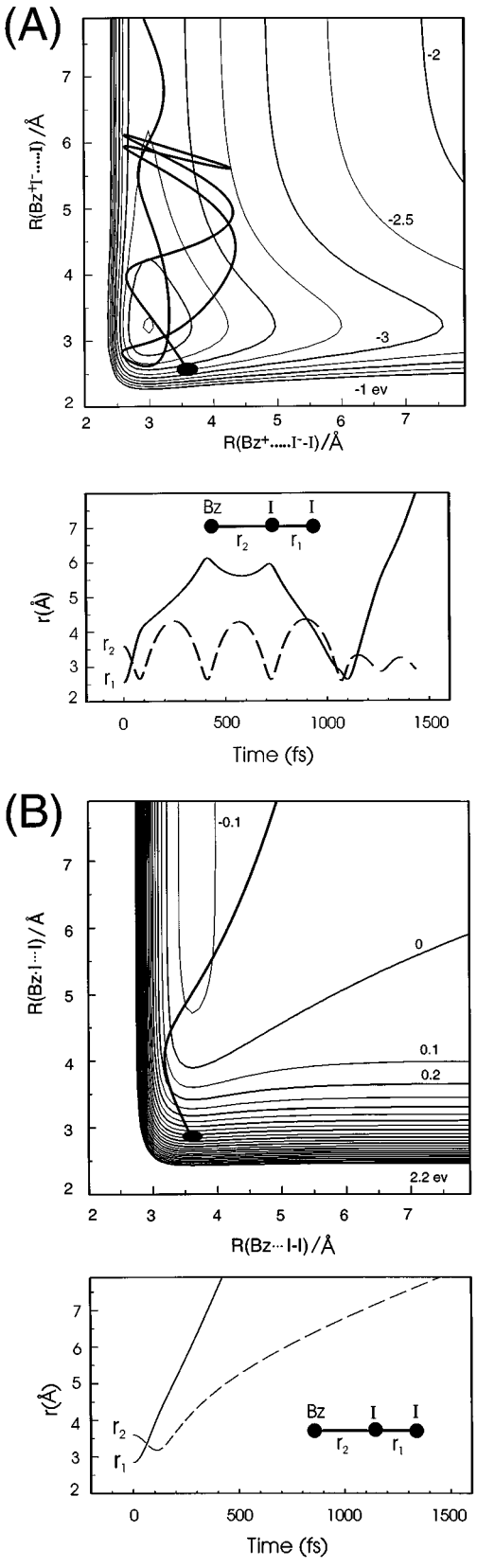

FIG. 26. (A) Upper panel: Ionic PES contour map along with a typical trajectory from MD calculations. Lower panel: time–distance plot of the trajectory shown in the upper panel. (B) A typical trajectory on the neutral PES. Note the different time scales for the Bz–I and I–I dissociations.

Vibrational excitation is seen in the $Bz^+ \cdot I^-$ product. It is interesting to note that these values are in accordance with the experimental results.

2. The neutral channel: Caging

The PES for the neutral channel is produced by combining Bz–I vdW and I–I repulsive potentials. The forms of the potentials are:

$$V_1(r_1) = A \exp\left(-\frac{r_1}{L}\right), \quad V_2(r_2) = \frac{C_{12}}{r_2^{12}} - \frac{C_6}{r_2^6}. \tag{14}$$

The parameters for V_1 are $A = 300eV$ and $L = 0.5$ Å, which are typical results from fitting the curves drawn by Mulliken for the I_2 repulsive states in Ref. 56. The parameters for V_2 are $C_{12} = 5.875 \times 10^5$ eV Å^{12} and $C_6 = 540$ eV Å.^{6} These were obtained by assuming a vdW well depth of 1000 cm^{-1} and an equilibrium D–I separation of 3.6 Å. The available energies are assumed to be localized in the I–I bond and are adjusted by initiating the trajectories at three different I–I separations to match the available energies of three dissociation asymptotes. Trajectories were calculated for several representative Bz–I separations between 3.2 and 4.0 Å, resembling a distribution of the ionic–neutral crossing points.

The results can be summarized as follows. For the I*+I* dissociation asymptote $v = 900$–1000 m/s, $\tau = 380$–440 fs (for the uncaged iodine atoms); $v = 300$–475 m/s, $\tau = 850$–1500 fs (for caged iodine atom if initial $r_2 = 3.6$–4.0 Å, Bz·I is bound if initial $r_2 = 3.2$–3.4 Å). For the I*+I dissociation asymptote $v = 1200$–1350 m/s, $\tau = 310$–335 fs (for the uncaged iodine atom); $v = 350$–780 m/s, $\tau = 570$–1700 fs (for the caged iodine atom). Finally for the I+I dissociation asymptote $v = 1480$–1600 m/s, $\tau = 270$–290 fs (for the uncaged iodine atom); and $v = 400$–730 m/s, $\tau = 470$–700 fs (for the caged iodine atom). A typical trajectory is shown in Fig. 26(B).

These results clearly show two distinct components both in the recoil speed (translational energy) and the dissociation times. In particular, the I*+I* and I+I* channels produce speeds that quantitatively agree with our measurements (note the distinct two components in each channel for velocity and reaction time). An interesting result is that some trajectories give bound D·I complexes. These trajectories all start from a short Bz–I separation. The probability for Bz·I complexes to survive the dissociation is probably smaller in reality. The reason is that if the I_2 dissociation occurs at short Bz–I separation, a significant fraction of the available energy might stay in the Bz–I coordinate after the ultrafast ionic–neutral switching. Therefore, there is more energy for the Bz–I dissociation. Overall, it is satisfactory to see that MD simulations, with simple potentials, give a consistent picture of the dynamics and mechanism.

G. Comparison with liquid phase and cluster studies

1. Liquid phase studies

In this section, an attempt is made to bridge the dynamics of the isolated reaction to those in clusters and liquids. In the gas phase and in solutions, the CT spectra are clearly evident as shown in Fig. 4. With ps resolution, Langhoff *et al.*[40(a)] and Hilinski *et al.*[40(b)] explored the dynamics of these complexes and showed the ultrafast nature of the reaction, though not resolved. Two fs studies of $D \cdot I_2$ reactions in the liquid phase have been reported recently by the groups of Wiersma[41,42] and Sension.[43] Here, we will discuss these results and compare the initial dynamics (<1 ps) reported in solutions with our findings. Long-time dynamics due to recombination and vibrational relaxation in solutions are not considered here.

Using a CPM laser system, Lenderink *et al.*[41] excited the complexes in I_2/mesitylene and I_2/toluene solutions at 310 nm and probed the photoproducts over the wavelength range from 400 to 700 nm. When they probed at 620 nm, they found that the transient absorption of the D·I complex rose within 25 fs. A transient absorption spectrum characteristic of molecular I_2 in solutions was also observed to appear on the same time scale, suggesting an impulsive fragmentation along the D–I_2 coordinate. Lenderink *et al.*[41] concluded that the excited complex branches into two different channels through parallel exit routes in 25 fs. The major channel (75%) involves breaking up of the $D \cdot I_2$ into its constitute molecules of D and I_2. In the other channel, the D–I complex and an iodine atom are formed.

The fs study reported by Pullen *et al.*[43] focused on the reactions of CT complexes in I_2/mesitylene solutions. Using a Ti:saphire laser system, they excited the complexes at 400 nm and probed the products at wavelengths ranging from 400 to 750 nm. The characteristic transient absorption spectrum of the mesitylene·I complex was found to be fully developed within 500 fs of the pump pulse. The authors also concluded that photodissociation occurs along both the mesitylene·I_2 and the I–I coordinates with a branching ratio of 2:3. The time scale for the bond breaking was estimated to be $\leqslant$250 fs in this study. Both studies indicated that the dissociations occur in both $D \cdot I_2$ and I–I coordinates on a very short time scale of 25–250 fs. The difference in the time scales of reactions could be simply due to the different excitation wavelengths. As pointed out by Pullen *et al.*,[43] the 310 and 400 nm excitation are, respectively, in the blue and red ends of the I_2/mesitylene solution CT absorption band. Sension's group has also measured transient absorption and anisotropy decay of hexamethylbenzene·I_2 in solutions and concluded that the complex has an oblique, nearly axial, geometry in alkanes. This result is consistent with our conclusion discussed in Sec. V C.

We have recently used a Ti:saphire amplified system and obtained the transient absorption by exciting I_2/mesitylene solution at 400 nm and probing the reaction at 620 nm.[78] We too see a rise within 100 fs and confirm the form of the transient reported by Lenderink *et al.*[41] The extremely rapid birth of the D·I complex in solutions following the CT excitation is consistent with the ultrafast ionic–neutral surface switching mechanism we proposed for the gas-phase $D \cdot I_2$ reactions.

In solutions, the $D \cdot I_2$ reaction centers are surrounded by solvent molecules. Following the ionic to neutral transition, the caged iodine atoms may remain bound to the donors and

are detected as D·I complexes because of the presence of other solvent molecules in the immediate vicinity. The transient absorption in solutions could therefore appear faster (25 fs)[41] than the buildup of the high-energy iodine atoms observed (450 fs) in our experiments. This is because the I–I separation does not need to be as large in solutions to develop the characteristic absorption of the D·I complexes (in our case, iodine atoms have to be separated far enough to be detected as a free iodine atom by the mass spectrometry). Furthermore, the random solute–solvent orientations in solutions can enhance the ionic–neutral state mixing and therefore increase the dissociation rates. The opening of the neutral channel produces ground state D·I complexes in solution and this is consistent with the fact that transient absorption observed in solution and gas phases has been assigned as due to ground state absorption of D·I, not $D^+ \cdot I^-$. Thus, the comparisons discussed above show that the initial dynamics of $D \cdot I_2$ reactions in the isolated gas phase is similar to that in solutions.

Another interesting result obtained by Lenderink *et al.*,[41] and confirmed by us, is that a slower rise ($t = 400$ fs) was also observed following the rapid initial rise of 25 fs. They attributed this to the additional mesitylene–I complexes that are formed by iodine atoms launched into the solvent and which subsequently react with other solvent molecules. Their interpretation is strongly supported by the observation that the 400 fs component is much less intense in mixed mesitylene/alkane solutions where fewer mesitylene molecules are available to react with. This picture is very similar to the caged iodine atom in our case, since it is the one that directly faces a solvent molecule as the impulsive dissociation of I_2 occurs. Our results show that it takes about 1 ps for the iodine atom to escape from the solvent force field. In solutions, the bouncing iodine atom are surrounded by more solvent molecules which can rapidly cool it down translationally such that it is finally bound to a specific solvent molecule. This process should take a shorter time than the complete cage exit.

An important exit channel considered in solutions is the dissociation along the $D–I_2$ coordinate. By measuring a transient absorption in the visible, both groups suggested that this process takes place very rapidly, as fast as the formation of D·I product. Although we have no information on the transient I_2 formation, we believe that this channel is relatively less in the isolated 1:1 complex. However, the neutral channel in the 1:1 complex would lead to some I_2 formation. In the presence of large solvent bath, the dissociating I_2 molecules can be caged rapidly (translational cooling) and a fast geminate recombination may take place on the sub-ps time scale as, e.g., in the case of I_2 in Ar solvent.[79] With the aid of solvent perturbation, nonadiabatic couplings to the ground state can lead to bound, vibrationally hot I_2 molecules. This kind of nonadiabatic processes can be very fast in solutions, although vibrational relaxation is typically on the ps time scale. For example, the reverse process of I_2 B-state predissociation, a slow process in the gas phase, has been shown to occur in ~200 fs in solution[80] and this time scale is determined by the nonadiabatic coupling between the B state and the repulsive potentials.

2. Cluster studies

We have previously reported[23] on the iodine atom transients when solvation with benzene is increased. The observed behavior at high benzene concentrations, Fig. 7(B), was related to the cage exit dynamics in large $(Bz)_n \cdot I_2$ clusters.[23] It was concluded that two distinct types of cluster solvations are present: one in which both iodine atoms are caged by the solvent molecules and the other for which only one iodine atom is caged. These structures were considered with the reactive pathway determined by the harpoon channel. In view of the contribution of the neutral channel we shall consider both channels in our discussion here.

Under high benzene concentration conditions, a broad size distribution of clusters is present in the molecular beam, as clearly manifested by the TOF-MS spectra shown in Fig. 7(A). The iodine atoms detected under such conditions thus come from a wide range of clusters of different sizes and structures. Yet, the observed transients exhibit distinct biexponential behaviors which is robust under all experimental conditions. The evolution of the transients is clearly accompanied by the change of the size distribution of clusters in the beam. These observations provide some clues to the fundamental architecture of the clusters.

First, the much slower rise components ($\tau \sim 20–75$ ps) observed under cluster conditions [Figs. 7(b)–7(e)] suggest a structure that is very different from the 1:1 complex. We attribute this slow-rise component to those complexes in which the two iodine atoms are both caged. Since the one-molecule caging time is on the order of 1.4 ps and the back electron transfer releases at least 1 eV of energy, we believe that the solvent cage which gives rise to the slow component must be sufficiently large. The evolution of the time constants of the slow-rise component from 20 to 75 ps and their relative weights are a manifestation of the increase of the averaged cluster size in the beam, consistent with the corresponding TOF-MS spectra.

As discussed earlier in this paper, the initial apparent rise observed in the 1:1 complex is a synthesis of two components: an extremely fast one (450 fs) arising from the prompt dissociation of the uncaged iodine atom and a slower one ($\tau \sim 1.4$ ps) which comes from the caged iodine atom. As the cluster size increases [Figs. 7(b)–7(e)], the initial apparent rise also becomes slower reaching longer than 2 ps. We attribute the initial rise to those trajectories in which at least one iodine atom is not caged by the solvent molecules. These include cluster structures with an incomplete solvent shell and with I_2 bound to the surface of a pure solvent cluster. In this architecture, the uncaged iodine atoms are still able to dissociate from the complexes freely without direct interactions with the rest of the system, although they may take a longer departing time due to the stronger vdW attraction resulting from the larger solvent clusters. After dissociation, the caged iodine atoms encounter, instead of a single solvent molecule, a cluster of solvent molecules, which should sig-

nificantly slow down the escape of the caged iodine atoms. For small clusters ($n=2,3$), the dissociation times of the caged iodine atoms are expected to be slightly longer than those in the 1:1 complex. For larger clusters, they may take significantly longer times to escape the solvent clusters and therefore can contribute to the slow components. Trapping of the caged iodine atoms in large clusters is also possible.

In addition to monitoring the escaped iodine atoms, we have also followed the initial CT state dynamics in large clusters by monitoring the transient signal directly from parent $(Bz)_n \cdot I_2^+$ mass channels ($n=1-4$) under large cluster conditions. The successful detection of the transient signal in these parent mass channels is due to the lower IPs and fragmentation of the larger cluster cations, and therefore each transient is likely to be a hybrid of transients arising from clusters larger than the one monitored. Transients observed from $n=1$ to 4 mass channels are almost identical and are dominated by an extremely fast decay with a similar time scale to those observed for the 1:1 complex. This result clearly shows that, although the cage exit takes tens of ps, the initial motion in the transition state is so fast such that the system moves out of the probing window in ~200 fs even in large clusters. The result is completely consistent with the solution results where the reaction is found to be ultrafast (25–250 fs) even when I_2 is surrounded by a large number of solvent molecules.

In summary, the two time scales observed in the iodine atom transients can be assigned to the caged and uncaged iodine atoms present in the clusters studied here. This characteristic is remarkably persistent from the 1:1 complex to the large $(Bz)_n \cdot I_2$ clusters, providing important insights into the solvation structure as well as cage exit dynamics. The fs initial state decay observed in large clusters indicates the ultrafast nature of the motion in the transition state. The distinct solvent structures found here have analogy in theoretical studies made recently on, e.g., $HF(Ar)_n$,[81] $I_2(Ar)_n$,[82] and $I_2^-(CO_2)_n$.[83]

VI. CONCLUSION

In this contribution, we have studied the transition state of CT reactions of 1:1 donor (D)–acceptor (A) complexes of benzene and its deuterated and methyl substituted species with iodine, isolated in a molecular beam, using fs transition-state spectroscopy and time-resolved kinetic-energy mass spectrometry. The CT transition state was directly reached by fs excitation and the dynamics were followed by monitoring either the product buildup or the initial state decay. Upon CT preparation of the complexes, free iodine atoms were found to appear very rapidly, on a time scale of less than 1 ps for all systems studied. The initial transition state decays extremely fast (~250 fs) and exhibits a biexponential behavior in the $Bz \cdot I_2$ case.

The translational energy distributions of the iodine atom products exhibit two distinct components: one peaks at a low energy (less than 1000 cm^{-1}) and the other at a high energy of about 5000 cm^{-1}. The two components also show different temporal behaviors: the high-energy one rises very rapidly (450 fs), whereas the low-energy component builds up much more slowly (1.4 ps). The recoil anisotropy (β) was measured for the two distributions. From these experiments, we obtained the direction of recoil relative to the direction of the transition moment, 30°–35°, indicating that the transition state structure is nearly axial, oblique.

The elementary dynamics involve two exit channels, namely the ionic and covalent pathways, Bz^+I^-+I and BzI+I, respectively. After fs initiation of the CT, the prepared wave packet quickly moves on the CT surface and bifurcates near the ionic–neutral interaction region. Some portion of the population continues on the adiabatic, harpooning potential. The remaining, larger portion of the wave packet population then quickly (250 fs) switches to the neutral repulsive surface through an intermolecular back electron transfer, leading to a direct I+I dissociation. The uncaged iodine atom dissociates freely and gives rise to the rapid (450 fs) high-translational-energy component. The caged iodine atom, on the other hand, encounters the electron donor molecule and slowly escapes from its force field with significant loss in its translational energy. At the interaction region, a small portion of the wave packet population transmits into the trapping well formed by the avoided crossing of the ionic and neutral surfaces. The trapped wave packet then slowly decays (~800 fs) by proceeding through the ionic exit or transmitting back to the lower neutral surface. MD simulations and descriptions of the HOMO/LUMO orbital interactions support our picture.

The present study reveals the complexity involved in the reaction dynamics of a seemingly simple system, studied for more than a half-century, whose initial state spectra or product-state yields do not permit the elucidation of the dynamics in the transition-state region or indicate the nature of the ionic-covalent channels. Through the studies in collisionless environments and with the aid of fs temporal and translational-energy resolutions, the dynamics can be revealed and the structure elucidated. The ability of fs time resolution to initiate the reaction wave packet from a well-defined region of intermolecular separations is critical to such studies. This work promises other applications, including different reactions, solvation dynamics, and CT reactions on or near surfaces. Solvation in clusters and liquids were introduced here and will be detailed in a forthcoming publication. Future works will also include studies of MD from the gas to the liquid[84] and the analogous systems of dissociative electron attachment[85] and ion–molecule reactions.[86]

ACKNOWLEDGMENTS

This work is supported by a grant from the National Science Foundation and the US Air Force Office of Scientific Research. We wish to thank Julius Su for his effort on the *ab initio* work which resulted in the structure in Fig. 2, Ju Guo for helping with the result on the mesitylene–iodine $\tau^{\ddagger}$ measurement, and Manish Gupta for helpful suggestions.

APPENDIX: FEMTOSECOND RESOLVED KINETIC ENERGY DISTRIBUTIONS

The KETOF technique is basically the mass spectrometric version of the Doppler photofragment spectroscopy implemented by laser-induced fluorescence (LIF). The subject has been extensively reviewed by many authors.[87] Here, we only discuss some of the important points relevant to the fs resolution introduced to KETOF and present the procedures used in the data analysis. We treat the product velocity distribution resulting from photoinitiated reactions in bimolecular complexes equivalently as that resulting from the photodissociation of a ''supermolecule.'' This is justified because the orientation of the CT transition dipole is well-defined in the complex molecular frame.

When a molecule is dissociated through a one-photon excitation by linearly polarized light, the c.m. angular distribution of fragments having the same recoil speed is axially symmetric with respect to the electric vector $\hat{\epsilon}$ of the light and can be expressed as[88]

$$I(\theta)=\frac{1}{4\pi}[1+\beta P_2(\cos\ \theta)], \tag{A1}$$

where θ is the angle between the final recoil direction and $\hat{\epsilon}$, $P_2(x)=1/2(3x^2-1)$ is the second Legendre polynomial, and β is the recoil anisotropy parameter. If the molecule dissociates instantaneously (much faster than a rotation period), then β is given by

$$\beta=2P_2(\cos\ \varphi), \tag{A2}$$

where φ is a fixed angle between the transition dipole moment (μ) of the molecule and the fragment recoil direction. β can have values between 2 and -1, corresponding to purely parallel ($\varphi=0$) and perpendicular ($\varphi=\pi/2$) transitions, respectively. In reality φ can be a range of angles due to rotational and/or vibrational motions which usually reduce the absolute magnitude of β. In these cases, an effective anisotropy parameter, β_{eff}, is more appropriate. A special case present in this work is the fragments produced by ''intracomplex scattering'' where a broad range of φ is expected.

In our experiment, the three-dimensional recoiling distribution is projected onto an axis defined in the laboratory frame, i.e., the TOF-MS axis. Transforming the angular distribution to the laboratory coordinate system in which the z axis is the TOF-MS axis gives the projected distribution as[89]

$$f(v_z,\chi)=\frac{1}{2v}\left[1+\beta P_2(\cos\ \chi)P_2\left(\frac{v_z}{v}\right)\right],\quad v_z\leqslant v,$$
$$f(v_z,\chi)=0,\quad v_z>v, \tag{A3}$$

where v_z is the velocity component along the z axis, v is the speed of the fragments, and χ is the angle between the z axis and the pump–laser polarization $\hat{\epsilon}$. The appearances of the v_z distributions thus depend on both χ and β. Figure 27 shows some theoretical v_z distributions at three pump–laser polarization angles.

In cases where the instrumental response function is negligible, the v_z distribution is directly related to the observed KETOF distribution by

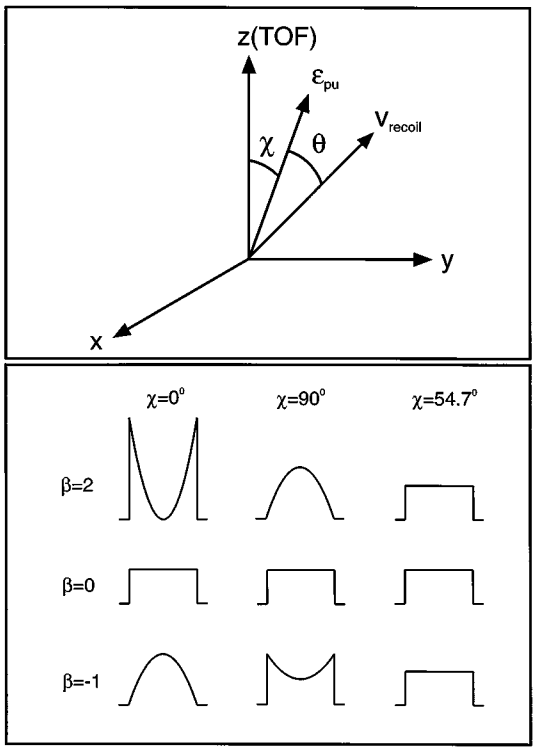

FIG. 27. *Upper*: Coordinate system used in describing the photofragment angular–velocity distribution in the KETOF experiment. ϵ_{pu} is the electric vector of the fs pump laser pulse and **V** recoil is the fragment recoil direction. *Lower*: Theoretical predictions of v_z distributions for some representative β's and χ's for single speed fragments. Note the distributions for $\beta=0$ and $\chi=54.7°$ are identical.

$$f(v_z)=h(T)\left|\frac{dT}{dv_z}\right|,$$
$$v_z=-\frac{qE}{m}(T-T_0), \tag{A4}$$

where $h(T)$ is the observed KETOF distributions, $(dT/dv_z)=-m/qE$ is merely an instrument constant for a given mass m, E is the extraction field strength, q is the ion charge, T_0 is the TOF for $v_z=0$ ions (apart from a small shift), and T is the TOF. Strictly speaking, the v_z distribution thus obtained is the laboratory v_z distribution. In our experiment, the c.m. of the dissociating system is traveling with the molecular beam whose z velocity component is negligible. This is because the molecular beam axis is orthogonal to the TOF-MS axis and the molecular beam is skimmed and detected at a far distance from the nozzle (~15 cm). Therefore, the laboratory v_z is equivalent to the $v_{z,\text{cm}}$, the iodine atom v_z with respect to the c.m. of the reaction precursor. As mentioned in Sec. III, a pair of deflection plates is used to correct the ion trajectories for the transverse drift introduced by molecular beam velocity. The force exerted on the ions by the deflection field is perpendicular to the z axis and therefore again do not interfere the $v_{z,\text{cm}}$ distribution.

If the dissociation results in a distribution of recoil speed $g(v)$, then we have to sum all the single speed v_z distribu-

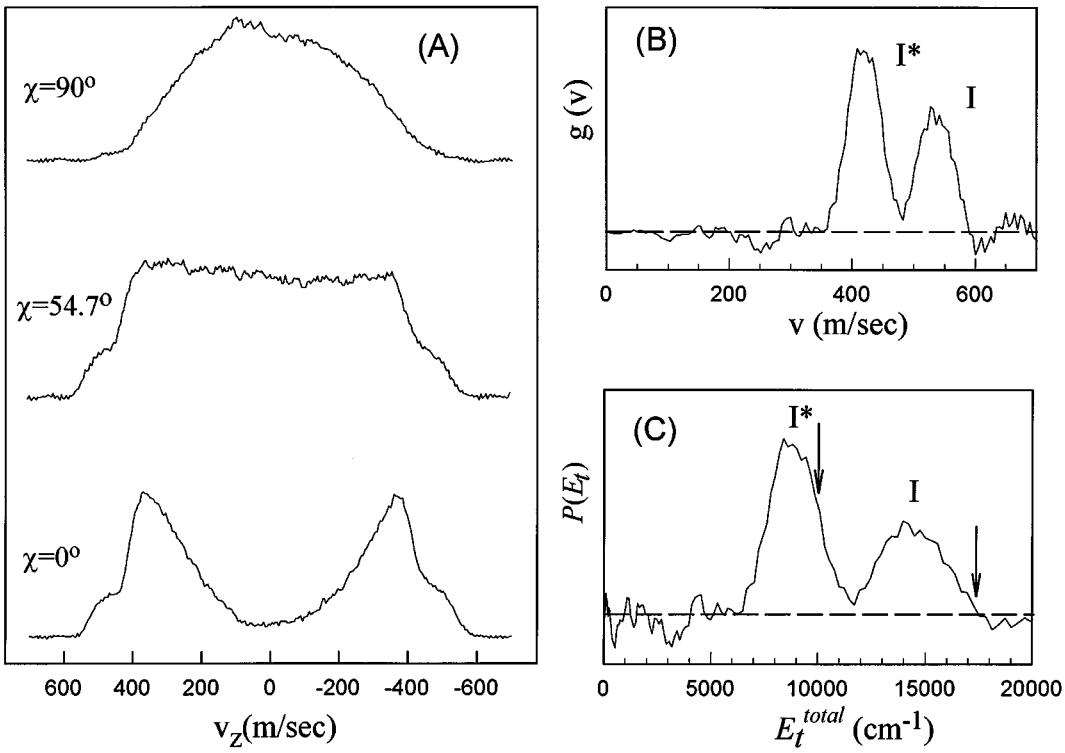

FIG. 28. (A) KETOF (v_z) distributions resulting from CH_3I photodissociation at 277 nm measured at three angles between the pump laser polarization and the TOF-MS axis. (B) Recoil speed distribution of the fragment iodine atoms derived from the magic angle data in (A). (C) Total product c.m. translational energy distribution of the CH_3I photodissociation transformed from (B). The two arrows indicate the available energy for producing I and I*.

tion [Eq. (A3)] over the entire speed distribution. The v_z distribution becomes

$$f(v_z,\chi)=\int_{|v_z|}^{\infty}\frac{g(v)dv}{2v}\left[1+\beta(v)P_2(\cos\chi)P_2\left(\frac{v_z}{v}\right)\right]. \tag{A5}$$

The observed KETOF distribution is then the convolution of $f(v_z,\chi)$ with some instrumental response functions. The task here is to extract $g(v)$ and $\beta(v)$ from the observed KETOF distribution. An important simplification to the above expression occurs when the KETOF distribution is measured at $\chi=54.7°$, or the ''magic angle.''[90] At this angle, $P_2(\cos\chi)=0$ and therefore the distribution is independent of β (see Fig. 27), i.e.,

$$f(v_z,54.7°)=\int_{|v_z|}^{\infty}\frac{g(v)dv}{2v}. \tag{A6}$$

In the present work, we measured KETOF distributions at the magic angle with respect to the TOF-MS axis to obtain $f(v_z,54.7°)$. The speed distribution $g(v)$ can then be directly obtained by differentiation:

$$g(v)=-2v\,\frac{d}{dv_z}f(v,54.7°)|_{v_z=v}. \tag{A7}$$

We tested this method by measuring the iodine atom KETOF distribution resulting from photodissociation of CH_3I at 277 nm. The probe laser wavelength was at 304.5 nm for the 2+1 REMPI iodine atom detection. It is well-known that upon excitation of CH_3I near our pump laser wavelength the C–I bond undergoes a direct dissociation due to the $n\rightarrow\sigma^*$ excitation.[91] The recoil anisotropy has been measured to be $\sim$1.8,[47] very close to the limiting value for a parallel transition. Figure 28(A) shows the v_z distributions measured at three different pump–laser polarization angles. These distributions are transformed from the corresponding KETOF distributions according to Eq. (A4). The χ dependencies of the v_z distributions qualitatively agree with the predictions for a parallel transition with very high β (see Fig. 27).

The v_z distribution measured at the magic angle is then smoothed by a Savitzky–Golay numerical filter[92] to remove the high-frequency noise. The resulting data are then differentiated according to Eq. (A7) to obtain the speed distribution shown in Fig. 28(B). Only the first-half of the KETOF data was used in the analysis. The data smoothing process is necessary because the differentiation significantly amplifies the noise.

The speed distribution thus obtained is the iodine atom speed distribution with respect to the c.m., which can be transformed to the translational energy distribution $P(E_t)$ by $P(E_t)=g(v)(dv/dE_t)$. In Fig. 28(C), we show the *total product translational energy* distribution in the c.m. frame obtained from the following relations:

$$E_{t,\mathrm{cm}}^{\mathrm{total}}=\frac{1}{2}\left(\frac{m_{\mathrm{I}}M}{M-m_{\mathrm{I}}}\right)v^2,\quad P(E_{t,\mathrm{cm}}^{\mathrm{total}})=\frac{g(v)}{v}\left(\frac{M-m_{\mathrm{I}}}{Mm_{\mathrm{I}}}\right), \tag{A8}$$

where m_{I} is the mass of the iodine atom (or the mass of the

detected ion in general) and M is the parent mass. In all CT reaction results presented in this paper, the dissociation kinematics is not as clear as the photodissociation of CH_3I (two-body dissociation) and may not even be uniform throughout the entire distribution. In such cases, only the relative translational energy of the iodine atom with respect to the c.m. is evaluated by the following relations:

$$E_{t,\mathrm{cm}}=\frac{1}{2}\,m_1 v^2, \quad P(E_{t,\mathrm{cm}})=\frac{g(v)}{v}\left(\frac{1}{m_1}\right). \tag{A9}$$

The speed distribution derived for the CH_3I photodissociation at 277 nm clearly exhibits two peaks. Similar distributions have been observed in a high-resolution photofragment translational spectroscopy experiment[93] in which the iodine atoms were detected by electron impact ionization in a mass spectrometer. Photodissociation of CH_3I has been reported to produce both the ground state (I, $^2P_{2/3}$) and the spin-orbit excited (I*, $^2P_{1/2}$) iodine atoms. We assigned these two peaks to I and I* atoms and calibrate the instrumental parameter (qE/m) according to the literature values. The calibrated parameter is within 10% of the value derived from our direct, but crude, measurements of the extraction field strength. The solid arrows in Fig. 28(C) indicate the upper limits of the total product translational energy released for both I and I* channels based on the reported CH_3I dissociation limits. The quantum yield of I* in the photodissociation of CH_3I at 266 nm has been reported to be 78%[94] or 73%±4%,[95] but decreases to ~0.05% at 308 nm[96] or ~43% at 304 nm.[50] Our measurement at 277 nm using fs lasers gives ~60% for the I* yield, indicating that our probe laser bandwidth indeed allows simultaneous detection of both I and I* with roughly equal sensitivities.

Note that the instrumental response is not deconvoluted in the results presented here. In our experiment, dissociation and ionization are achieved by fs laser pulses and the resulting ions are detected by MCPs. As a result, a mass peak originates from a direct ionization of a parent molecule under very low signal level conditions has a width of ~4 ns (FWHM) detected by the digital oscilloscope at a sampling rate of 2.5 gigasamples per second. This translates into an instrument-limited speed resolution of ~20 m/s, which is not significant in the present work. Although this instrument-limited resolution is independent of speed, it gives rise to a speed dependent translational energy resolution. Other factors, such as diffraction off the ion optics grids and inhomogeneity of the electric fields, may also affect the resolution. Overall, the observed FWHM of~60 m/s for the I* channel provides an upper limit for the speed resolution at $v=400$ m/s.

An important energy resolution limiting factor in the fs KETOF experiment is the broad bandwidth of the fs lasers. Our pump laser has a bandwidth (FWHM) of ~4 nm, or ~500 cm^{-1} at 277 nm. This introduces a broad distribution to the available energies for dissociations and reactions and is probably as important as other instrument-limited factors. The width for the I* component is ~2500 cm^{-1} (FWHM). A high resolution photofragment translational spectroscopic study[93] has shown that photodissociation of CH_3I at 266 nm using a narrow bandwidth ns laser produces a distribution of ~1200 cm^{-1} FWHM for the I* channel due to the excitation of the umbrella mode of the CH_3 fragment. This comparison gives a rough idea of the overall energy resolution we have in measuring the total product translational energy. Note that the 500 cm^{-1} energy uncertainty is related to the total available energy. For the translational energy of the iodine atom with respect to the c.m. measured for the $D\cdot I_2$ reactions; the energy uncertainty could be much smaller, depending on the fraction of the available energy that is channeled into translational energy of the iodine atom. This is especially true for the low-energy components which are probably the results of a small fraction of the total available energy. In summary, we believe that the instrument response and laser bandwidth should not affect our interpretation of the data. However, one should keep in mind that these smearing factors are present in the derived translational energy distributions.

For the $D\cdot I_2$ reactions, the anisotropy parameter distribution $\beta(v)$ is obtained by fitting the v_z distributions measured at parallel polarization using the speed distributions derived from the magic angle data. The entire anisotropy distribution (0–1400 m/s) is divided into a certain number of ''bins.'' Each bin covers a speed range of 100 m/s and the anisotropy is assumed to be constant within each single bin. The fitting procedure is based on a nonlinear least square fitting algorithm,[92] adjusting the value in each bin to obtain a best fit to the parallel polarization v_z distribution according to Eq. (A5).

[1] P. Y. Cheng, D. Zhong, and A. H. Zewail, J. Chem. Phys. **103**, 5153 (1995).
[2] N. F. Scherer, L. R. Khundkar, R. B. Bernstein, and A. H. Zewail, J. Chem. Phys. **87**, 1451 (1987); I. R. Sims, M. Gruebele, E. D. Potter, and A. H. Zewail, *ibid.* **97**, 4127 (1992).
[3] A. H. Zewail, Science **242**, 1645 (1988).
[4] T. S. Rose, M. J. Rosker, and A. H. Zewail, J. Chem. Phys. **91**, 7415 (1989).
[5] J. A. Syage, P. M. Felker, and A. H. Zewail, J. Chem. Phys. **81**, 2233 (1984).
[6] S. K. Kim, J. J. Breen, D. M. Willberg, L. W. Peng, A. Heikal, J. A. Syage, and A. H. Zewail, J. Phys. Chem. **99**, 7421 (1995).
[7] E. D. Potter, J. L. Herek, S. Pedersen, Q. Liu, and A. H. Zewail, Nature **66**, 355 (1992).
[8] C. Dedonder-Lardeux, M. Berdah, C. Jouvet, S. Martrenchard-Barra, J. M. Mestdagh, D. Solgadi, and J. P. Visticot, J. Chem. Phys. **104**, 2740 (1996).
[9] H. A. Benesi and J. H. Hildebrand, J. Am. Chem. Soc. **71**, 2703 (1949).
[10] R. S. Mulliken, J. Am. Chem. Soc. **72**, 610 (1950); **74**, 811 (1952).
[11] R. S. Mulliken and W. B. Person, *Molecular Complexes: A Lecture and Reprint Volume* (Wiley-Interscience, New York, 1969).
[12] K. Liu, J. C. Polanyi, and S. Yang, J. Chem. Phys. **96**, 8628 (1992); **98**, 5431 (1993); J. C. Polanyi and J. X. Wang, J. Phys. Chem. **99**, 13691 (1995).
[13] R. B. Metz, S. E. Bradforth, and D. M. Neumark, Adv. Chem. Phys. **81**, 1 (1992); D. M. Neumark, Annu. Rev. Phys. Chem. **43**, 153 (1992).
[14] P. Hering, P. R. Brooks, R. F. Curl, R. S. Judson, and R. S. Lowe, Phys. Rev. Lett. **44**, 687 (1980); P. R. Brooks, Chem. Rev. **88**, 407 (1988).
[15] M. Boivineau, J. Le Calvé, M. C. Castex, and C. Jouvet, Chem. Phys. Lett. **128**, 528 (1986); **130**, 208 (1986); J. Chem. Phys. **84**, 4712 (1986).
[16] C. Jouvet, M. Boivineau, M. C. Duval, and B. Soep, J. Phys. Chem. **91**, 5416 (1987).
[17] T. O. Nelson, D. W. Setser, and J. Qin, J. Phys. Chem. **97**, 2585 (1993).
[18] S. I. Ionov, G. A. Brucker, C. Jaques, L. Valachovic, and C. Wittig, J. Chem. Phys. **99**, 6553 (1993); S. A. Wright, M. F. Tuchler, and J. D. McDonald, Chem. Phys. Lett. **226**, 570 (1994); R. D. van Zee and J. C. Stephenson, J. Chem. Phys. **102**, 6946 (1995).

[19] St. J. Dixon-Warren, E. T. Jensen, J. C. Polanyi, G. Q. Xu, S. H. Yang, and H. C. Zeng, Faraday Discuss. Chem. Soc. **91**, 451 (1991).
[20] J. C. Polanyi and A. H. Zewail, Acc. Chem. Res. **28**, 119 (1995).
[21] J. M. Saveánt, Adv. Phys. Org. Chem. **26**, 1 (1990).
[22] L. Eberson, Acta Chem. Scand. Ser. B **36**, 533 (1982); L. Eberson, *Electron Transfer Reactions in Organic Chemistry* (Springer, Berlin, 1987).
[23] P. Y. Cheng, D. Zhong, and A. H. Zewail, Chem. Phys. Lett. **242**, 369 (1995).
[24] E. Beckmann, Z. Phys. Chem. **5**, 76 (1889).
[25] M. W. Hanna, J. Am. Chem. Soc. **90**, 285 (1968); M. W. Hanna and J. Lippert, in *Molecular Complexes*, edited by R. Foster (Elek Science, London, 1973), and references therein.
[26] L. J. Andrews, Chem. Rev. **54**, 713 (1954); S. McGlynn, Chem. Rev. **58**, 1113 (1958).
[27] *Spectroscopy and Structure of Molecular Complexes*, edited by J. Yarwood (Plenum, New York, 1973); *Molecular Complexes*, edited by R. Foster (Elek Science, London, 1973).
[28] E. M. Voigt and B. Meyer, J. Chem. Phys. **49**, 852 (1968).
[29] F. T. Lang and R. L. Strong, J. Am. Chem. Soc. **87**, 2345 (1965).
[30] D. Atack and O. K. Rice, J. Phys. Chem. **58**, 1017 (1954).
[31] T. D. McLean, B. B. Ratcliff, J. Z. Pastalan, and K. K. Innes, J. Quantum. Spectrosc. Radiat. Transfer **42**, 445 (1989).
[32] E. Kochanski and J. Prissette, Nouv. J. Chim. **4**, 509 (1980).
[33] J. Su and A. H. Zewail (work in progress). These calculations indicate a near-flat potential for iodine or benzene, consistent with x-ray structural findings for similar systems (see Ref. 35).
[34] E. E. Ferguson, J. Chem. Phys. **25**, 577 (1956).
[35] O. Hassel and K. O. Strømme, Acta. Chem. Scand. **12**, 1146 (1958); *ibid*. **13**, 1781 (1959).
[36] L. Fredin and B. Nelander, J. Am. Chem. Soc. **96**, 1672 (1974).
[37] J. C. Schug and M. C. Dyson, J. Chem. Phys. **58**, 297 (1973); J. C. Schug and K. A. Levinson, Theor. Chim. Acta **37**, 269 (1975); I. Jano, *ibid*. **66**, 341 (1985).
[38] T. A. Gover and G. Porter, Proc. R. Soc. London, Ser. A **262**, 476 (1961); S. J. Rand and R. L. Strong, J. Am. Chem. Soc. **82**, 5 (1960); N. Yamamoto, T. Kajikawa, H. Sato, and H. Tsubomura, *ibid*. **91**, 265 (1969).
[39] V. A. Brosseau, J. R. Basila, J. F. Smalley, and R. L. Strong, J. Am. Chem. Soc. **94**, 716 (1972).
[40] (a) C. A. Langhoff, K. Gnädig, and K. B. Eisenthal, Chem. Phys. **46**, 117 (1980); (b) E. F. Hilinski and P. M. Rentzepis, J. Am. Chem. Soc. **107**, 5907 (1985).
[41] E. Lenderink, K. Duppen, and D. A. Wiersma, Chem. Phys. Lett. **211**, 503 (1993).
[42] E. Lenderink, K. Duppen, F. P. X. Everdij, J. Mavri, R. Torre, and D. A. Wiersma, J. Phys. Chem. (in press).
[43] S. Pullen, L. A. Walker II, and R. J. Sension, J. Chem. Phys. **103**, 7877 (1995).
[44] L. A. Walker II, S. Pullen, B. Donovan, and R. J. Sension, Chem. Phys. Lett. **242**, 177 (1995).
[45] M. J. Rosker, M. Dantus, and A. H. Zewail, J. Chem. Phys. **89**, 6113 (1988).
[46] A. H. Zewail, *Femtochemistry: Ultrafast Dynamics of the Chemical Bound* (World Scientific, Singapore, 1994), and articles therein.
[47] G. E. Hall, N. Sivakumar, R. Ogorzalek, G. Chawla, H. P. Haerri, P. L. Houston, I. Burak, and J. W. Hepburn, Faraday Discuss. Chem. Soc. **82**, 13 (1986); R. Ogorzalek Loo, G. E. Hall, H. P. Haerri, and P. L. Houston, J. Phys. Chem. **92**, 5 (1988).
[48] H. J. Hwang, J. Griffiths, and M. A. El-Sayed, Int. J. Mass Spectrom. Ion Processes **131**, 265 (1994).
[49] S. M. Penn, C. C. Hayden, K. J. Carlson Muyskens, and F. F. Crim, J. Chem. Phys. **89**, 2909 (1988).
[50] R. A. Hertz and J. A. Syage, J. Chem. Phys. **100**, 9265 (1994).
[51] M. Mons and I. Dimicoli, J. Chem. Phys. **90**, 4037 (1989).
[52] T. Baumert, S. Pedersen, and A. H. Zewail, J. Phys. Chem. **97**, 12447 (1993).
[53] P. Y. Cheng, D. Zhong, and A. H. Zewail, Chem. Phys. Lett. **237**, 399 (1995).
[54] P. Y. Cheng, D. Zhong, and A. H. Zewail, J. Phys. Chem. **99**, 15733 (1995).
[55] After the benzene vapor was shut off, pure He was allowed to flow over the iodine crystals through the gas lines for a short period of time, typically 10–30 min depending on the donors until no benzene parent ion could be seen in the TOF-MS. This procedure removed adsorbed benzene.
[56] R. S. Mulliken, J. Chem. Phys. **55**, 288 (1971).
[57] E. R. Bernstein, in *Atomic and Molecular Clusters*, edited by E. R. Bernstein (Elsevier, New York, 1990).
[58] C. N. Rao, G. C. Chaturvedi, and S. N. Bhat, J. Mol. Spectrosc. **33**, 554 (1970).
[59] J. Birks, *Photophysic of Aromatic Molecules* (Wiley, New York, 1970), and references therein.
[60] L. Asbrink, E. Lindholm, and O. Edqvist. Chem. Phys. Lett. **5**, 609 (1970).
[61] E. C. M. Chen and W. E. Wentworth, J. Phys. Chem. **89**, 4099 (1985).
[62] A. Engdahl and B. Nelander, J. Chem. Phys. **78**, 6563 (1983).
[63] K. D. Raner, J. Lusztyk, and K. U. Ingold, J. Phys. Chem. **93**, 564 (1989).
[64] Ch. A. Brau, in *Excimer Lasers*, edited by C. K. Rhodes (Springer, Berlin, 1979).
[65] J. K. Ku and D. W. Setser, in *Photochemistry and Photophysics above 6 eV*, edited by F. Lahmani (Elsevier, Amsterdam, 1985).
[66] R. J. Donovan *et al.*, Faraday Discuss. Chem. Soc. **84**, 221 (1987).
[67] D. R. Herschbach, Adv. Chem. Phys. **10**, 319 (1966); J. L. Kinsey, G. H. Kwei, and D. R. Herschbach, J. Chem. Phys. **64**, 2133 (1976).
[68] J. Li and K. Balasubramanian, J. Mol. Spectrosc. **138**, 162 (1989); C. Teichteil and M. Pelissier, Chem. Phys. **180**, 1 (1994).
[69] J. Segall, Y. Wen, C. Wittig, A. Garcia-Vela, and R. B. Gerber, Chem. Phys. Lett. **207**, 504 (1993); C. Jaques, L. Valachovic, S. Ionov, E. Bohmer, Y. Wen, J. Segall, and C. Witting, J. Chem. Soc. Faraday Trans. **89**, 1419 (1993).
[70] R. B. Gerber, A. B. McCoy, and A. Garcia-Vela, Annu. Rev. Phys. Chem. **45**, 275 (1994).
[71] G. Porter and J. A. Smith, Proc. R. Soc. London, Ser. A **261**, 28 (1961); R. L. Strong, J. Phys. Chem. **66**, 2423 (1962).
[72] R. L. Strong and J. Perano, J. Am. Chem. Soc. **89**, 2535 (1967).
[73] R. B. Bernstein, *Chemical Dynamics via Molecular Beam and Laser Techniques* (Oxford University Press, Oxford, 1982).
[74] R. A. Marcus and N. Sutin, Biochim. Biophys. Acta **811**, 265 (1985); *Photoinduced Electron Transfer*, edited by M. A. Fox and M. Chanon (Elsevier, Amsterdam, 1988).
[75] T. S. Rose, M. Rosker, and A. H. Zewail, J. Chem. Phys. **91**, 7415 (1989).
[76] D. M. Willberg, M. Gutmann, J. J. Breen, and A. H. Zewail, J. Chem. Phys. **96**, 198 (1992).
[77] G. N. Robison, R. E. Continetti, and Y. T. Lee, J. Chem. Phys. **89**, 6226 (1988).
[78] C. Wan, M. Gupta, and A. H. Zewail (unpublished).
[79] J. K. Wang, Q. Liu, and A. H. Zewail, J. Phys. Chem. **99**, 11309 (1995); Q. Liu, J. K. Wang, and A. H. Zewail, *ibid*. **99**, 11321 (1995).
[80] N. F. Scherer, D. M. Jonas, and G. R. Fleming, J. Chem. Phys. **99**, 153 (1993).
[81] T. Schröder, R. Schinke, S. Liu, Z. Bacic, and J. W. Moskowit, J. Chem. Phys. **103**, 9228 (1995).
[82] C. C. Martens, in *Femtochemistry, the Lausanne Conference*, edited by M. Chergui (World Scientific, Singapore, 1996).
[83] J. M. Papanikolas, P. E. Maslen, and R. Parson, J. Chem. Phys. **102**, 2452 (1995).
[84] Y. Danten, B. Guillot, and Y. Guissani, J. Chem. Phys. **96**, 3782 (1992).
[85] I. Hahndorf, E. Illenberger, L. Lehr, and Jörn Manz, Chem. Phys. Lett. **231**, 460 (1994).
[86] D. M. Cyr, C. G. Bailey, D. Serxner, M. G. Scarton, and M. A. Johnson, J. Chem. Phys. **101**, 10507 (1994).
[87] G. E. Hall and P. L. Houston, Annu. Rev. Phys. Chem. **40**, 375 (1989), and references therein.
[88] R. N. Zare and D. R. Herschbach, Proc. IEEE **51**, 173 (1963); R. N. Zare, Mol. Photochem. **4**, 1 (1972).
[89] R. Vasudev, R. N. Zare, and R. N. Dixon, J. Chem. Phys. **80**, 4863 (1984).
[90] J. L. Kinsey, J. Chem. Phys. **66**, 2560 (1977); M. Dubs, U. Brühlmann, and J. R. Huber, *ibid*. **84**, 3106 (1986).
[91] R. S. Mulliken, J. Chem. Phys. **8**, 382 (1940).
[92] W. H. Press, B. P. Flannery, S. A. Teukolsky, and W. T. Vetterling, *Numerical Recipes* (Cambridge University Press, New York, 1992).
[93] R. K. Sparks, K. Shobatake, L. R. Carlson, and Y. T. Lee, J. Chem. Phys. **75**, 3838 (1981).
[94] S. J. Riley and K. R. Wilson, Faraday Discuss. Chem. Soc. **53**, 132 (1972).
[95] W. P. Hess, S. J. Kohler, H. K. Haugen, and S. R. Leone, J. Chem. Phys. **84**, 2143 (1986).
[96] S. L. Baughcum and S. R. Leone, J. Chem. Phys. **72**, 6531 (1980).